SECURITY CLASSIFICATION OF THIS PAGE *(When Data Entered)*

REPORT DOCUMENTATION PAGE

READ INSTRUCTIONS BEFORE COMPLETING FORM

1. REPORT NUMBER: NRL Report 7839	2. GOVT ACCESSION NO.
3. RECIPIENT'S CATALOG NUMBER	
4. TITLE *(and Subtitle)*: CHARACTERISTICS OF CRACK PROPAGATION AT THE INTERFACE BETWEEN TWO DISSIMILAR MEDIA	5. TYPE OF REPORT & PERIOD COVERED: Final report on one phase of a continuing problem.
	6. PERFORMING ORG. REPORT NUMBER
7. AUTHOR(s): D. R. Mulville	8. CONTRACT OR GRANT NUMBER(s)
9. PERFORMING ORGANIZATION NAME AND ADDRESS: Naval Research Laboratory, Washington, D.C. 20390	10. PROGRAM ELEMENT, PROJECT, TASK AREA & WORK UNIT NUMBERS: NRL Problems F01-04 and F01-14, Projects RR 023-03-45-5451 and SF 54-544-701-12432
11. CONTROLLING OFFICE NAME AND ADDRESS: F01-04 Department of the Navy, Office of Naval Research, Arlington, Va. 2217 (Continued)	12. REPORT DATE: February 26, 1975
	13. NUMBER OF PAGES: 58
14. MONITORING AGENCY NAME & ADDRESS*(if different from Controlling Office)*	15. SECURITY CLASS. *(of this report)*: Unclassified
	15a. DECLASSIFICATION/DOWNGRADING SCHEDULE

16. DISTRIBUTION STATEMENT *(of this Report)*

Approved for public release; distribution unlimited.

17. DISTRIBUTION STATEMENT *(of the abstract entered in Block 20, if different from Report)*

18. SUPPLEMENTARY NOTES

19. KEY WORDS *(Continue on reverse side if necessary and identify by block number)*

Complex variable	Interfacial Failure
Photoelasticity	Crack Propagation
Strain-energy release rate	Surface Roughness
Stress analysis	Debonding
	Residual Stress

20. ABSTRACT *(Continue on reverse side if necessary and identify by block number)*

An analysis was made of the stresses along a bonded interface between two dissimilar materials. Various loading conditions that give rise to interfacial crack propagation were considered, including thermal loads, bending loads, and tensile loads parallel to the bond. From this two-dimensional stress analysis, the strain-energy release rate $\mathcal{G}_c$ was formulated as a fracture criterion for interfacial failure.

(Continued)

DD FORM 1 JAN 73 1473 EDITION OF 1 NOV 65 IS OBSOLETE
S/N 0102-014-6601

SECURITY CLASSIFICATION OF THIS PAGE *(When Data Entered)*

11. Controlling Office name and address (Continued)

F01-14 Department of the Navy
Naval Ship Systems Command
Washington, D.C. 20362

20. Abstract (Continued)

Studies were conducted on specimens of epoxy bonded to aluminum. The effect of surface roughness of the aluminum on fracture toughness was measured for four different surface finishes. It was found that increased surface roughness resulted in greater fracture toughness. This may be explained by the observation that the interfacial cracks replicated the surface features of the aluminum. Microscopic studies of the failure surfaces indicate that crack propagation occurs in the epoxy near the interface, and that a residue of epoxy remains bonded to the aluminum. The magnitude of the residual stresses due to casting and curing of the epoxy was determined by photoelastic techniques. Methods were developed for analyzing the birefringent pattern in the epoxy to determine the magnitude of the elastic residual stress and the frozen stress. It was found that residual stresses can contribute 15% to 20% of the strain required for crack initiation at the interface.

CONTENTS

INTRODUCTION 1

THEORETICAL ANALYSIS 3

- Problem Formulation 3
- Problem Solution 8
- Strain-Energy Release Rate Formulation 10
- Limitations of the Theoretical Analysis 15

EXPERIMENTAL INVESTIGATION 16

- Specimen Geometry and Loading 16
- Photoelastic Observations 17
- Instrumented Specimen 24
- Crack-Propagation Studies 30

RESULTS AND DISCUSSION 34

- Results of Crack-Propagation Studies 34
- Fracture-Surface Observations 39

SUMMARY AND CONCLUSIONS 39

ACKNOWLEDGMENTS 43

REFERENCES 43

APPENDIX A—Experimental Procedure and Analysis 46

CHARACTERISTICS OF CRACK PROPAGATION AT THE INTERFACE BETWEEN TWO DISSIMILAR MEDIA

INTRODUCTION

Because of their strength and ease of fabrication, bonded materials and composites are being used more and more in aircraft and other modern engineering structures. However, many problems, such as debonding and delamination, are associated with the use of these materials. In the following, a review of previous theoretical analyses of interfacial problems is presented along with a description of the experimental studies which have addressed these problems.

The plane problem of a crack between dissimilar materials was first considered by Williams [1]. Using an eigenfunction approach, he analyzed the stresses near the tip of a crack between two dissimilar isotropic materials joined without residual stress. It was found that the resulting stresses possess an oscillatory character of the form $(1/\sqrt{r})\sin(\lambda \log r)$ and $(1/\sqrt{r})\cos(\lambda \log r)$, where r is the radial distance from the crack tip and λ is a function of material properties. This is in contrast to the homogeneous problem, in which the form of the resulting stresses near the crack tip is a $1/\sqrt{r}$ type of singularity.

Erdogan [2] considered similar problems using Muskhelishvili's [3] solutions in terms of complex potential functions. His results verify the oscillatory behavior of the stresses described by Williams. He extended the solution by defining a pair of stress-intensity factors related to the Griffith-Irwin fracture theory. In the homogeneous problem, the stress-intensity factors K_I and K_{II} are associated with symmetric (normal) and skew-symmetric (shear) stress fields, respectively. However, for the nonhomogeneous problem considered here, each of the stress-intensity factors is related to both symmetric and skew-symmetric stress fields. Later Erdogan [4] analyzed the general plane problem of a series of through cracks along the interface subjected to known surface tractions and known dislocations in displacement along the bonded segments. His solutions included, for example, the following problems: residual stresses due to bonding, stresses due to loading parallel to the bonded segment, wedge loading on the surface of a cut, and stresses due to thermal loading. Erdogan [5] also examined the axisymmetric problem of penny-shaped cracks and ring-shaped cavities at the interface of bonded dissimilar materials.

England [6] considered the plane problem of an internally pressurized crack between two dissimilar materials. He discussed the physical significance of the oscillatory behavior of the stresses and displacements near the crack tip. These oscillations implied that the upper and lower surfaces of the crack should wrinkle and overlap. He concluded that the oscillations predicted by the solution were confined to a very small region near the ends of the crack and that on physical grounds the solution should provide a good approximation at points remote from this region. Rice and Sih [7, 8] analyzed the bending of a bimaterial plate with cracks along the bond and later considered the general

Manuscript submitted October 21, 1974.

plane problem for interfacial cracks between dissimilar materials. Using a combination of the eigenfunction approach and the complex-variable method, they formulated a solution for the stress and displacement fields and defined the stress-intensity factors in terms of a complex potential function. Using Rice and Sih's stress function, Sawyers and Anderson [9] applied boundary collocation procedures to obtain stress-intensity factors for finite bimaterial plates. They defined an interfacial stress-intensity factor, and indicated that interfacial cracks will be stable for a fixed loading applied to one material parallel to the bond and unstable for fixed loading normal to the interface or for biaxial loading.

Fowlkes [10] presented a finite-element analysis of cracks in the region of a bi-material interface. He considered the several modes of failure that result as a crack approaches the interface and then proceeds along the bond or through the interface. Various stress-intensity factors are presented for these models, and they are related to failure in glass-reinforced composites. Lin [11] recently conducted a numerical study of the stress intensity of a crack at an interface between two materials. In his finite-element analysis he introduces a bimaterial crack element that spans both materials and encloses the crack tip.

Chou and Hirth [13] have determined the stress distribution in a bimaterial plate under antiplane and uniform compressive loading on a plane normal to the interface. They conclude that uniform compression on both materials induces tensile stresses near the end of the bond that may cause debonding at the interface.

Brown and Erdogan [13] analyzed thermal stresses in bonded materials with fully or partly insulated cavities at the interface. They found that whereas, shear stresses were dominant for the residual stress and isothermal problems, normal stresses became dominant in thermal-gradient problems. Recently, Erdogan and Gupta [14] considered the torsion problem of a disk bonded to a dissimilar shaft. Gotch [15], Clements [16], and Willis [17] have examined plane problems of cracks between dissimilar anisotropic materials.

While all these studies provided theoretical solutions to various interfacial problems for dissimilar materials, little experimental data were available to verify the results. Recently, Wu and Thomas [18] conducted an experimental study of crack propagation at the interface of a bimaterial plate with loading normal to the bond. Using Rice and Sih's [8] analysis they determined the stress-intensity factors for interfacial failure. The failure mode observed in their studies was a small amount of slow crack growth along the interface, followed by rapid crack propagation away from the interface, leading to ultimate fracture. Wang [19], using numerical techniques, analyzed the plane problem of an interfacial crack between adhesively bonded dissimilar materials. He also, conducted an experimental compliance calibration to verify the results of the numerical solutions. However, he did not include crack-propagation studies in his investigation.

Williams [20-22] has conducted both analytic and experimental debonding studies using a pressurized blister test. This test was designed to threat the case of a soft elastomeric material cast and cured on a relatively rigid substrate. A pressure inlet hole was drilled through the underside of the substrate, and pressure was applied to lift the elastomeric layer off the surface of the substrate, forming a blister. This technique was applied by Burton, et al [23], to study debonding of solid propellant and compatible liner from a rocket motor case. It has also been applied to measure the adhesive quality

of dental cements, paints, explosively welded metal parts, and barnacle cement. These applications are presented briefly in a recent paper by Bennett, et al. [24], in which he discusses the advantages and limitations of this test method. Its advantages are (a) ease of sample preparation, (b) ease of testing with relatively inexpensive equipment, and (c) determination of several data points from a single specimen. However, for some materials with higher adhesive strength than cohesive strength, failure often begins at the periphery of the blister and extends into the material rather than along the bond.

Although this sampling of analytical effort indicates that there has been considerable theoretical work on interfacial stress analysis, little has been done experimentally. Prior to this investigation, experimental studies had not been conducted for combinations of residual stresses, uniform thermal loading, external forces applied parallel to the bond, or external moments that cause interfacial failure, not did a formulation exist for the strain-energy release rate for interfacial failure under these combinations of loads. The objective of this study was to examine in detail the nature of the fracture process at the interface of two bonded dissimilar materials by studying experimentally crack propagation in bimaterial specimens subjected to a variety of loading conditions. For ease in illustrating the phenomena, one of the materials in the example will be considered as a relatively rigid body; i.e., the Young's modulus of one material is much greater than that of the other.

THEORETICAL ANALYSIS

Problem Formulation

In this section the stress field is analyzed for the plane problem of two bonded dissimilar materials with cracks along the interface. Both materials are assumed to be linearly elastic, homogeneous, and isotropic. These results are used to formulate the strain-energy release rate for crack propagation at the interface between the two materials. The theoretical development follows closely the methods and analysis of Milne-Thomson [25], and the results are compared with those obtained using a finite-element analysis.

Consider two elastic half-spaces S^L and S^R, as shown in Fig. 1, with a common boundary A along the entire x axis, the positive y axis being directed normally to the x axis and lying wholly in S^L. Let the segment A' of the x axis bounded by the end points $(-\ell, 0)$ and $(\ell, 0)$ correspond to an interfacial bond, with the remaining segment A'' on either side of A' representing two cracks. The boundary A separating S^L and S^R is the sum of A' and A''. Assume that each half-space is externally loaded by a system of self-equilibrating forces, with A'' traction-free. Under this loading, no resultant normal or shear forces are transferred across A'. In addition, assume that the difference between the strains in S^L and S^R on A' is specified.

If $t(-\ell \leqslant t \leqslant \ell)$ denotes a real parameter defining a point on A', then the boundary conditions can be expressed formally as

$$\widehat{yy}_1^L(t) - i\widehat{xy}_1^L(t) = \widehat{yy}_2^R(t) - i\widehat{xy}_2^R(t) = 0 \quad \text{on } A'' \tag{1}$$

$$\widehat{yy}_1^L(t) - i\widehat{xy}_1^L(t) = \widehat{yy}_2^R(t) - i\widehat{xy}_2^R(t) \quad \text{on } A' \tag{2}$$

$$[u_i(t) + iv_1(t)]'^L - [(u_2(t) + iv_2(t)]'^R = d'(t) \quad \text{on } A' \tag{3}$$

$$\int_A [\widehat{yy}_1^L(t) - i\widehat{xy}_1^L(t)]dt = X - iY = 0 \quad \text{on } A \tag{4}$$

where

$i = \sqrt{-1}$

$\widehat{yy}$ and $\widehat{xy}$ are normal and shear stresses, respectively

u and v are displacement components along the x and y axes, respectively

X and Y are the components of the resultant force on A

$d'(t)$ is a specified function of t.

Superscripts L and R refer to the values of the functions on A as approached from points in S^L and S^R, respectively. A function defined in S^L is denoted by subscript 1, and one defined in S^R by subscript 2.

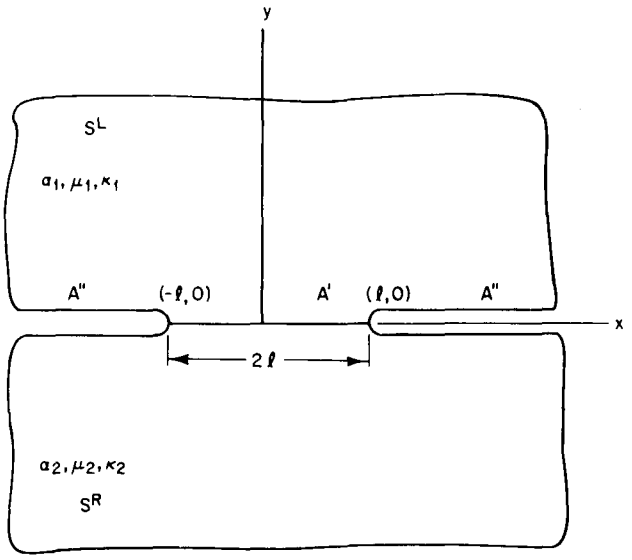

Fig. 1—Two elastic half-spaces bonded along A'

Equation (1) states that the surface tractions vanish along the unbonded section of the real axis A''. The second boundary condition, Eq. (2), states that the traction vector is continuous across A'. The third boundary condition, Eq. (3), states that the strain difference is specified on A'. Finally, Eq. (4) states that the components of the resultant force on A' are assumed to be zero.

Stresses and displacements can be written in terms of the complex stress functions $W_k(z)$ and $w_k(z)$, as follows:

$$\widehat{xx}_k + \widehat{yy}_k = W_k(z) + \overline{W}_k(\overline{z}) \tag{5}$$

$$\widehat{yy}_k - \widehat{xx}_k + 2i\widehat{xy}_k = \overline{z}W'_k(z) + w_k(z) \tag{6}$$

$$4\mu_k(u_k + iv_k) = \aleph_k \grave{W}_k(z) - z\overline{W}_k(\overline{z}) - \grave{w}_k(\overline{z}) \tag{7}$$

where

$z \in S^L$ for $k = 1$

$z \in S^R$ for $k = 2$

$\grave{W}_k(z) = \int W_k(z)dz$

$\grave{w}_k(z) = \int w_k(z)dz$.

In the above μ_k is the shear modulus, $\aleph_k = (3 - 4\nu_k)$ for plane strain, and $\aleph_k = (3 - \nu_k)/(1 + \nu_k)$ for generalized plane stress, where ν_k is Poisson's ratio.

By means of the following substitutions it is possible to extend the definition of $W_1(z)$ into S^R and $W_2(z)$ into S^L by analytically continuing $W_k(z)$ across the unloaded segment of the boundary A''. From Eq. (5) and (6), we have

$$2(\widehat{yy}_k - i\widehat{xy}_k) = W_k(z) + \overline{W}_k(\overline{z}) + z\overline{W}'_k(\overline{z}) + \overline{w}_k(\overline{z}) . \tag{8}$$

We may define $W_1(z)$ in S^R by setting $2(\widehat{yy}_k - i\widehat{xy}_k)$ equal to zero and replacing $\overline{z}$ by z. Thus in S^R

$$W_k(z) = -\overline{W}_k(z) - z\overline{W}'_k(z) - \overline{w}_k(z) , \tag{9}$$

and in S^L

$$W_k(\overline{z}) = -\overline{W}_k(\overline{z}) - \overline{z}\,\overline{W}'_k(\overline{z}) - \overline{w}_k(\overline{z})$$

or

$$\overline{w}_k(\overline{z}) = -W_k(\overline{z}) - \overline{W}_k(\overline{z}) - \overline{z}\overline{W}'_k(\overline{z}) . \tag{10}$$

Using this result in Eqs. (7) and (8), we may now write

$$2(\widehat{yy}_k - i\widehat{xy}_k) = W_k(z) - W_k(\overline{z}) + (z - \overline{z})\overline{W}'_k(\overline{z}) \tag{11}$$

$$4\mu_k(u_k + iv_k)' = \aleph_k W_k(z) + W_k(\overline{z}) - (z - \overline{z})\overline{W}'(\overline{z}) \tag{12}$$

where the stress combinations are expressed in terms of the single complex variable $W_k(z)$ in each half plane.

Consider now the stress and displacement boundary conditions, Eqs. (2) and (3) on A' in S^L. If in Eqs. (11) and (12) we let $z \to t$ from S^L, where $z \in S^L$, and $\bar{z} \to t$ from S^R, where $\bar{z} \in S^R$, then

$$2(\widehat{yy}_1 - i\widehat{xy}_1)^L = W_1^L(t) - W_1^R(t) \tag{13}$$

and

$$4\mu_1(u_1 + iv_1)'^L = \aleph_1 W_1^L(t) + W_1^R(t) . \tag{14}$$

Since we assumed that the resultant vector $X+iY$ of the external forces on A is zero, then for large values of $|z|$, using Eq. (4), we have

$$W_1(z) = O\left(\frac{1}{z^2}\right) \tag{15}$$

where O denotes "terms of the order of." Similarly for S^R, let $z \to t$ from S^R, where $z \in S^R$, and $\bar{z} \to t$ from S^L, where $\bar{z} \in S^L$. Thus

$$2(\widehat{yy}_2 - i\widehat{xy}_2)^R = W_2^R(t) - W_2^L(t) \tag{16}$$

and

$$4\mu_2(u_2 + iv_2)'^R = \aleph_2 W_2^R(t) + W_2^L(t) . \tag{17}$$

Also, for zero resultant forces and large values of $|z|$, from Eqs. (2) and (4), we obtain

$$W_2(z) = O\left(\frac{1}{z^2}\right) . \tag{18}$$

From the stress boundary condition (Eq. (2)) on A', we have, from Eqs. (13) and (16),

$$W_1^L(t) - W_1^R(t) = W_2^R(t) - W_2^L(t)$$

or

$$[W_1(t) + W_2(t)]^L - [W_1(t) + W_2(t)]^R = O . \tag{19}$$

Equation (25) implies that $W_1(z) + W_2(z)$ is analytic in the entire plane S^L and S^R, including the real axis. For large values of $|z|$, using Eqs. (15) and (18), we have

$$[W_1(z) + W_2(z)] = O\left(\frac{1}{z^2}\right) . \tag{20}$$

Therefore, the function $W_1(z) + W_2(z)$ is analytic and bounded in the plane, including the point at infinity, and by Liouville's theorem must reduce to a constant. The above expression shows that the function approaches zero at infinity, and hence must be zero in the entire plane. Thus $W_1(z) + W_2(z) = 0$ for all z, or

$$W_1(z) = -W_2(z) \tag{21}$$

From the displacement boundary condition (Eq. (3)), we have

$$(u_1 + iv_1)'^L - (u_2 + iv_2)'^R = d'(t)\,, \tag{22}$$

and substituting from Eqs. (14) and (17) results in

$$\frac{1}{4\mu_1}[\aleph_1 W_1^L(t) + W_1^R(t)] - \frac{1}{4\mu_2}[\aleph_2 W_2^R(t) + W_2^L(t)] = d'(t)\,. \tag{23}$$

Using Eq. (21) gives

$$\frac{1}{\mu_1}[\aleph_1 W_1^L(t) + W_1^R(t)] + \frac{1}{\mu_2}[\aleph_2 W_1^R(t) + W_1^L(t)] = 4d'(t)$$

or

$$a\,W_1^L(t) + b\,W_1^R(t) = 4\,d'(t) \tag{24}$$

where

$$a = \left(\frac{\aleph_1}{\mu_1} + \frac{1}{\mu_2}\right)$$

$$b = \left(\frac{1}{\mu_1} + 1\frac{\aleph_2}{\mu_2}\right).$$

This can be expressed as

$$c\,W_1^L(t) + W_1^R(t) = \frac{4d'(t)}{b}\,, \tag{25}$$

where $c = a/b$ is defined as the bielastic constant.

The displacement on A', $d(t)$, can be expressed as:

$$d(t) = (u_0^R - u_0^R) + i(v_0^L - v_0^R) + (\eta_R^L - \eta_R^R)t + (\eta_T^L - \eta_T^R)t + (\eta_M^L - \eta_M^R)t + i\frac{t^2}{2\mathrm{R}} \tag{26}$$

or

$$d(t) = u_0 + iv_0 + \eta t + i\frac{t^2}{2R} \tag{27}$$

and

$$d'(t) = \eta + i\frac{t}{R}, \tag{28}$$

where

$$u_0 = u_0^L - u_0^R \tag{29}$$

$$v_0 = v_0^L - v_0^R \tag{30}$$

$$\eta = (\eta_R^L - \eta_R^R) + (\eta_T^L - \eta_T^R) + (\eta_M^L - \eta_M^R). \tag{31}$$

In Eqs. (26) through (31), η_R is the strain due to residual stresses, η_T is the strain due to thermal loading, η_M is the strain due to mechanical loading, R represents the radius of curvature of A', and u_0 and v_0 merely represent translation of A' in the complex plane. Using Eq. (28) in Eq. (25), we have

$$c\,W_1^L(t) + W_1^R(t) = \frac{4}{b}\left(\eta + i\frac{t}{R}\right). \tag{32}$$

It now remains to solve Eq. (32) for the complex stress function and to determine the resulting stress components. From this result the strain-energy release rate G will be formulated for crack propagation at the materials' interface.

Problem Solution

Consider first the solution of the homogeneous equation

$$c\chi_1^L(t) + \chi_1^R(t) = O, \tag{33}$$

corresponding to Eq. (32). This equation has the form of a homogeneous Hilbert functional equation, and its solution can be expressed in terms of the Plemelj function on the arc $(-\ell, \ell)$:

$$\chi_1(z) = (z - \ell)^{\tau-1}(z + \ell)^{-\tau} \tag{34}$$

where

$$\tau = \frac{1}{2} + i\lambda$$

$$\lambda = (\log c)/2\pi .$$

Nonhomogeneous Eq. (32) can be solved by evaluating the integral

$$W_1(z) = \frac{\chi_1(z)}{2\pi i}\int_{-\ell}^{\ell}\frac{4}{bc}\left(\eta + i\frac{t}{R}\right)\frac{dt}{\chi_1^L(t)\,(t - z)} + P(z)\chi(z). \tag{35}$$

In evaluating this integral, we transformed it from a line integral into a Cauchy integral on a lancet around $(-\ell, \ell)$. Using the Cauchy integral theorem, we have

$$W_1(z) = \frac{4}{a+b}\left(\eta[1 - (z + 2i\lambda\ell)\chi(z)] + \frac{i}{R}\left\{z - \left[z^2 + 2i\lambda\ell z - \frac{1}{2}(1 + 4\lambda^2)\ell^2\right]\chi(z)\right\}\right) + P(z)\chi(z) \tag{36}$$

where $P(z)$ is a polynominal in z chosen such that $W(z)$ vanishes at infinity.

The stresses are determined by substituting Eqs. (36) and (34) into Eq. (13), which yields

$$\begin{aligned} 2(\widehat{yy}_1 - i\widehat{xy}_1)^L = \frac{4}{a+b}\Bigg(&\eta[1 - (t + 2i\lambda\ell)\chi_1^L(t)] \\ &+ \frac{i}{R}\left\{t - \left[t^2 + 2i\lambda\ell t - \frac{1}{2}(1 + 4\lambda^2)\ell^2\right]\chi_1^L(t)\right\} \\ &- \eta[1 - (t + 2i\lambda\ell)\chi_1^R(t)] \\ &- \frac{i}{R}\left\{t - \left[t^2 + 2i\lambda\ell t - \frac{1}{2}(1 + 4\lambda^2)\ell^2\right]\chi_1^R(t)\right\}\Bigg) . \end{aligned} \tag{37}$$

From Eq. (33), where $\chi_1^R(t) = -c\chi_1^L(t)$,

$$\begin{aligned} 2(\widehat{yy}_1 - i\widehat{xy}_1)^L = \frac{4}{a+b}\Bigg(&\eta[1 - (t + 2i\lambda\ell)\chi_1^L(t)] \\ &+ \frac{i}{R}\left\{t - \left[t^2 - 2i\lambda\ell t - \frac{1}{2}(1 + 4\lambda^2)\ell^2\right]\chi_1^L(t)\right\} \\ &- \eta\left[1 + \frac{a}{b}(t + 2i\lambda\ell)\chi_1^L(t)\right] \\ &- \frac{i}{R}\left\{t + \frac{a}{b}\left[t^2 + 2i\lambda\ell t - \frac{1}{2}(1 + 4\lambda^2)\ell^2\right]\chi_1^L(t)\right\}\Bigg) \end{aligned} \tag{38}$$

or

$$2(\widehat{yy}_1 - i\widehat{xy}_1)^L = -\frac{4}{b}\left\{\eta(t + 2i\lambda\ell) + \frac{i}{R}\left[t^2 + 2i\lambda\ell t - \frac{1}{2}(1 + 4\lambda^2)\ell^2\right]\right\}\chi_1^L(t) . \tag{39}$$

Expanding this equation using Eq. (34) yields

$$2(\widehat{yy}_1 - i\widehat{xy}_1)^L = -\frac{4}{b[(t+\ell)(t-\ell)]^{1/2}}\left\{\eta(t + 2i\lambda\ell) + \frac{i}{R}\left[t^2 + 2i\lambda\ell t - \frac{1}{2}(1 + 4\lambda^2)\ell^2\right]\right\}\left\{\cos\left[\lambda \log\left(\frac{t-\ell}{t+\ell}\right)\right] + i \sin\left[\lambda \log\left(\frac{t-\ell}{t+\ell}\right)\right]\right\} . \tag{40}$$

It should be noted that the resulting stresses in this analysis possess an oscillatory character similar to that mentioned in the preceding section. Also, this solution is similar to that presented by Erdogan [4] for residual stresses in bonded materials. Figures 2, 3, and 4 show the distribution of the stresses on the interface of various materials combinations for a value of $\eta = 10^{-4}$. This corresponds, for example, to a uniform tensile stress, $\widehat{xx}_2 = 1000$ psi, applied to an aluminum plate bonded to an unloaded epoxy plate, $E_2/E_1 = 20$, in Figs. 2 and 3. Figure 4 shows the resulting interfacial stresses for bending, $R = -5555$ in., applied to the same combination of materials.

Strain-Energy Release Rate Formulation

As shown in Fig. 5, the stress vector on S^L is

$$P_1(t) = [s_1(t) + ip_1(t)] \tag{41}$$

where

$$p_1(t) = -\widehat{yy}_1(t)$$

$$s_1(t) = -\widehat{xy}_1(t) .$$

On S^R, the stress vector is

$$P_2(t) = -[s_2(t) + ip_2(t)] \tag{42}$$

where

$$p_2(t) = -\widehat{yy}_2(t)$$

$$s_2(t) = -\widehat{xy}_2(t) .$$

Equations (41) and (42) can be written in the following form:

$$iP_1(t) = i[s_1(t) + ip_1(t)] = -[p_1(t) - is_1(t)] \tag{43}$$

and

$$-iP_2(t) = -i[s_2(t) + ip_2(t)] = -[p_2(t) - is_2(t)] . \tag{44}$$

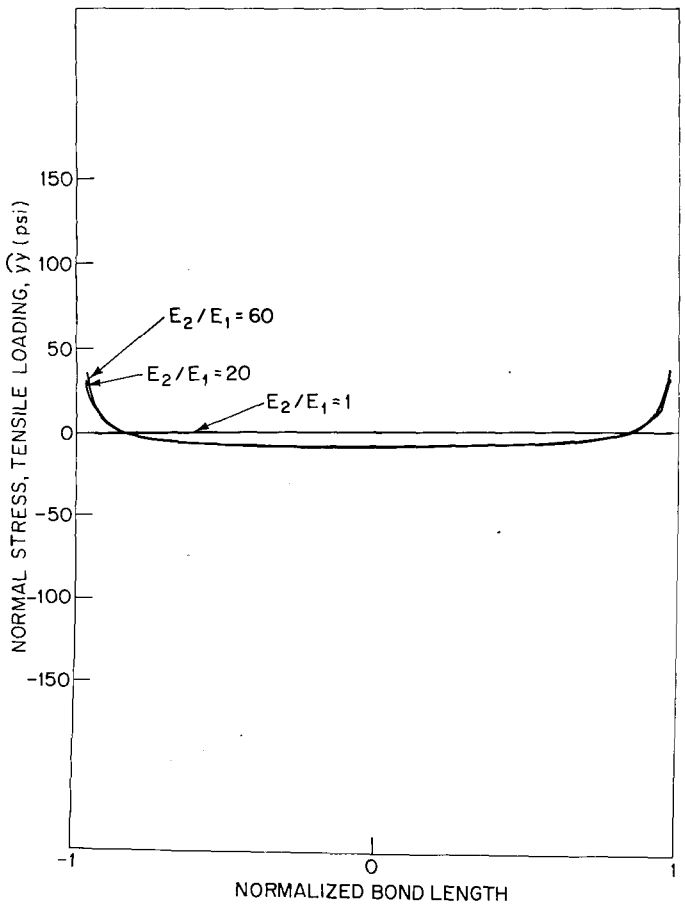

Fig. 2—Normal stresses along the bond under tensile loading

Imposing the stress boundary conditions on A' yields

$$iP_1(t) = -iP_2(t) , \tag{45}$$

and thus

$$P_1(t) + P_2(t) = O . \tag{46}$$

Consider the work U done by the stress vector acting along the bond $(-\ell, \ell)$, as follows:

$$U = \mathrm{Re}\frac{1}{2} \int_{-\ell}^{\ell} \left\{ P_1(t)[u_1(t) - iv_1(t)] + P_2(t)[u_2(t) - iv_2(t)] \right\} dt . \tag{47}$$

Imposing the displacement boundary condition (Eq. (3)) and the relation between the stress vectors (Eq. (45)) yields

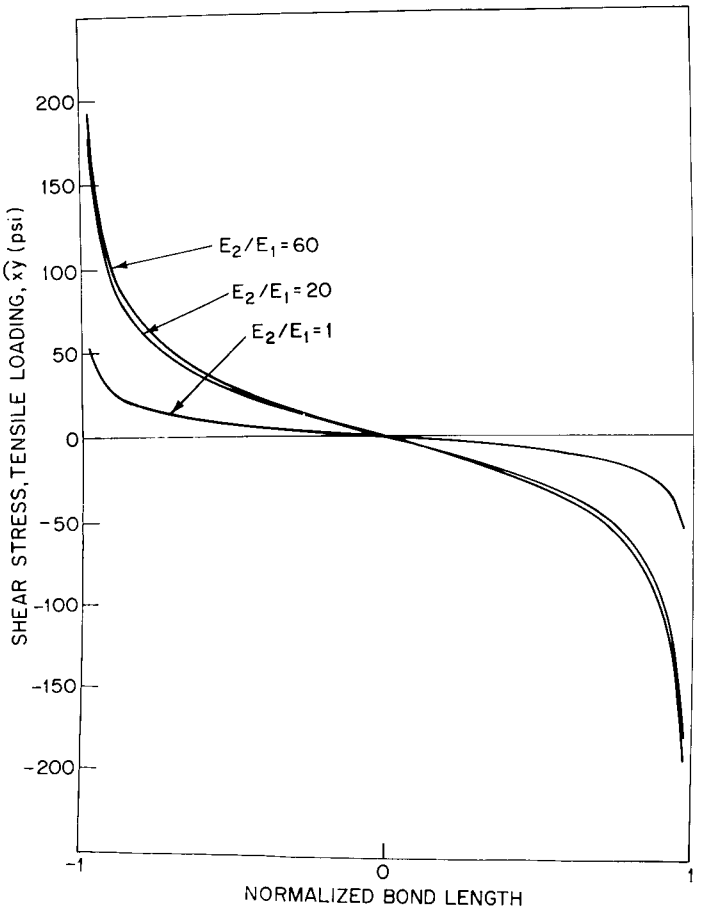

Fig. 3—Shear stresses along the bond under tensile loading

$$U = \mathrm{Re}\frac{1}{2}\int_{-\ell}^{\ell} P_1(t)\bar{d}(t)\,dt\,. \tag{48}$$

From the assumed $d(t)$ on A' Eq. (27) and Eq. (43),

$$U = \mathrm{Re}\left\{\frac{1}{2}\int_{-\ell}^{\ell} i[p_1(t) - is_1(t)]\left(u_0 - iv_0 + \eta t - i\frac{t^2}{2R}\right)dt\right\}$$

or

$$U = \mathrm{Re}\left\{\frac{i}{2}(u_0 - iv_0)\int_{-\ell}^{\ell}[p_1(t) - is_1(t)]\,dt\right.$$

$$\left. + \frac{i}{2}\int_{-\ell}^{\ell}[p_1(t) - is_1(t)]\left(\eta t - i\frac{t^2}{2R}\right)dt\right\}\,. \tag{49}$$

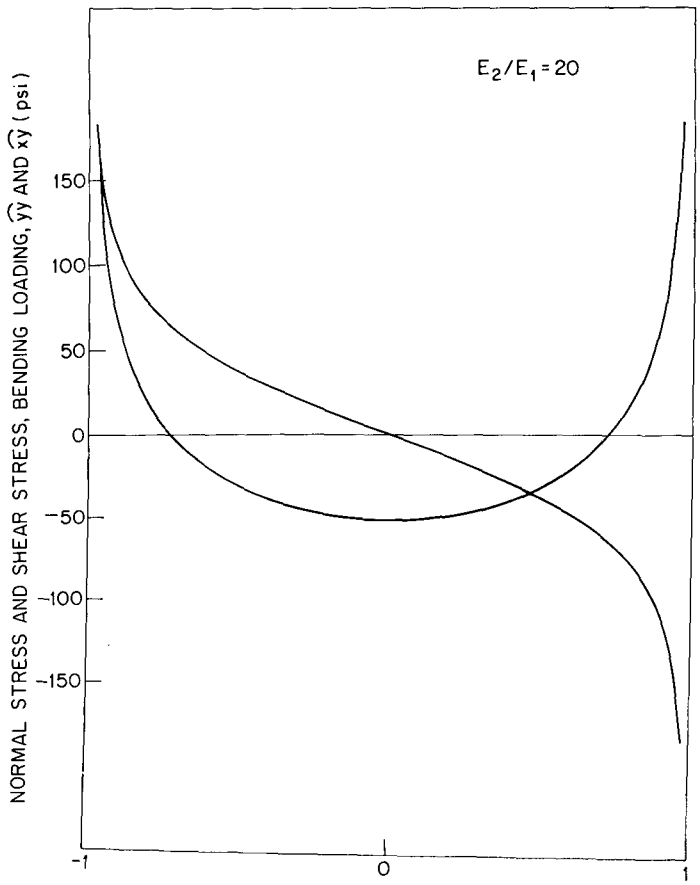

Fig. 4—Normal and shear stresses under bending loading

Using the resultant force boundary condition of Eq. (4) on A' causes the first integral to vanish. Using Eq. (39) allows the second integral to be written as

$$U = \text{Re}\left\{\frac{i}{b}\int_{-\ell}^{\ell}\eta(t + 2i\lambda\ell)\left(\eta t - i\frac{t2}{2R}\right)\chi_1^L(t)\,dt\right.$$

$$\left.+\frac{i}{b}\int_{-\ell}^{\ell}\frac{i}{R}\left[t^2 + 2i\lambda\ell t - \frac{1}{2}(1 + 4\lambda^2)\ell^2\right]\left(\eta t - i\frac{t^2}{2R}\right)\chi_1^L(t)\,dt\right\}.$$

Evaluating this integral yields

$$U = \frac{2\pi(1 + 4\lambda^2)}{a + b}\left[\frac{\eta^2\ell^2}{2} - \frac{2\eta\lambda\ell^3}{3R} + \frac{\ell^4}{16R^2}(1 + 4\lambda^2)\right]. \tag{51}$$

The strain-energy release rate $\mathcal{J}$ is defined as the decrease in stored elastic strain energy per unit of crack increase dm. Thus

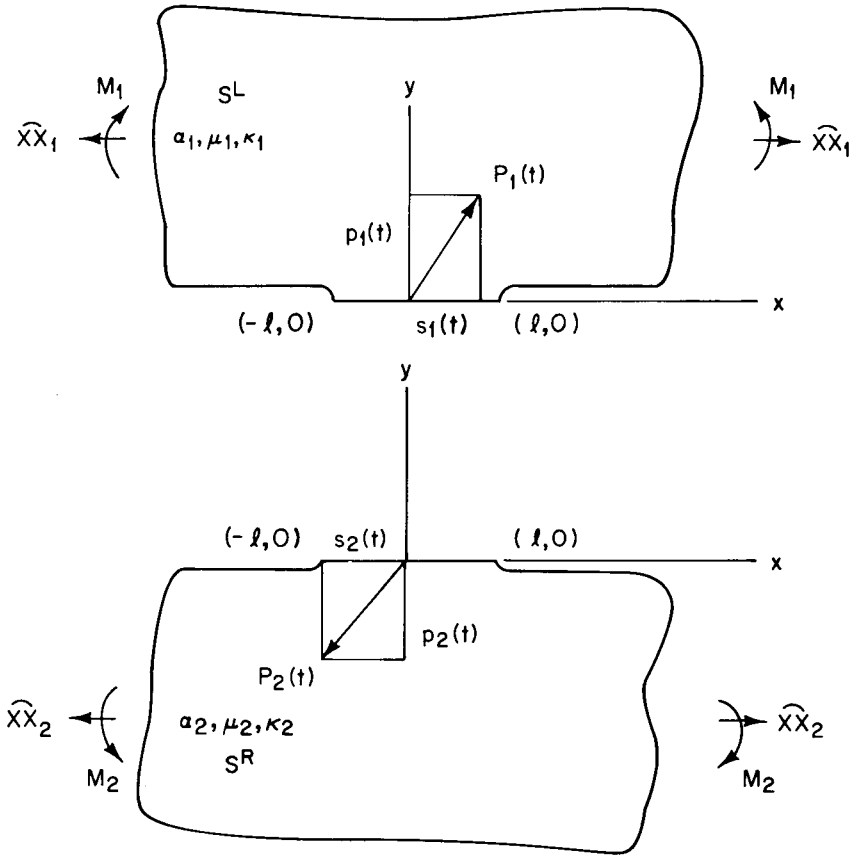

Fig. 5—Resultant stress vectors on upper and lower half-spaces

$$\mathcal{G} = -\frac{\partial U}{\partial m} = -\frac{\partial U}{\partial \ell}\frac{d\ell}{dm}. \tag{52}$$

From the geometry shown in Fig. 5, $d\ell/dm = -1$, and using Eq. (51) we have

$$\mathcal{G} = \frac{2\pi(1 + 4\lambda^2)}{a + b}\left[\eta^2\ell - \frac{2\eta\lambda\ell^2}{R} + \frac{\ell^3}{4R^2}(1 + 4\lambda^2)\right] \tag{53}$$

or

$$\mathcal{G} = \frac{2\pi(1 + 4\lambda^2)}{\left(\dfrac{\aleph_1 + 1}{\mu_1} + \dfrac{\aleph_2 + 1}{\mu_2}\right)}\left[\eta^2\ell - \frac{2\eta\lambda\ell^2}{R} + \frac{\ell^3}{4R^2}(1 + 4\lambda^2)\right]. \tag{54}$$

For generalized plane stress, $\aleph_k = (3 - \nu_k)/(1 + \nu_k)$ and $\mu_k = E_k/2(1 + \nu_k)$; therefore the strain-energy release rate formulation above can be expressed as

$$\mathcal{J} = \frac{\pi(1 + 4\lambda^2)}{4\left(\frac{1}{E_1} + \frac{1}{E_2}\right)} \left[\eta^2 \ell - \frac{2\eta\lambda\ell^2}{R} + \frac{\ell^3}{4R^2}(1 + 4\lambda^2)\right] , \tag{55}$$

and for plane strain $\aleph_k = 3 - 4\nu_k$. Thus

$$\mathcal{J} = \frac{\pi(1 + 4\lambda^2)}{4\left[\frac{(1 - \nu_1^2)}{E_1} + \frac{(1 - \nu_2^2)}{E_2}\right]} \left[\eta^2 \ell - \frac{2\eta\lambda\ell^2}{R} + \frac{\ell^3}{4R^2}(1 + 4\lambda^2)\right] . \tag{56}$$

These expressions for the strain-energy release rate are based on the plane problem of two elastic half-spaces bonded along A' and can be used to analyze the following loading conditions: residual stresses, uniform thermal loading, forces applied parallel to the bond to one or both half-spaces, bending loads applied to one or both half-spaces or any combination of these loads.

To assess the effect of finite boundaries on this solution, a finite-element analysis was conducted for tensile loading parallel to the bond and for bending loads applied to one half-space. The specimen geometry used in these numerical analyses was selected on the basis of the experimental studies described in the second section. Results of the finite-element analysis are presented in Appendix A.

Limitations of the Theoretical Analysis

In the preceding analysis, both materials were assumed to be linearly elastic, homogeneous, and isotropic. While these assumptions are useful for analysis, they often do not adequately describe the behavior of real materials. In the following experimental section, epoxy-aluminum bonded specimens are subjected to external loading that results in interfacial crack propagation. At room temperature this epoxy system behaves in a linear elastic manner, but at temperatures approaching the postcure temperature of 125°F, the behavior becomes viscoelastic. The preceding analysis does not describe the stress or displacement field for viscoelastic media, nor does the fracture-mechanics analysis account for time-dependent behavior.

In addition to problems that may be caused by the viscoelastic nature of the materials, there are problems caused by viscous flow or nonlinear behavior in the vicinity of the crack tip. Irwin [26] proposed corrections to the linear elastic theory that account for plastic flow at the crack tip. Essentially, his approach was to add a plasticity adjustment, obtained from estimates of the size of the plastic zone, to the linear elastic solution. Orowan [27] postulated that plastic deformation is always present in a thin layer next to the surface of fracture in a normally ductile material even if the fracture appears completely brittle. He proposed replacing the surface energy term in the Griffith formula with a factor related to the plastic work per unit of area of the surface of fracture. For brittle fracture, Orowan [28] suggests that many independent cracks are initiated and arrested and that this mechanism raises the work of crack propagation far above the surface energy. Fracture-surface observations, described in the next section, indicated that the interfacial crack is composed of multiple fractures, which replicate the surface features of the aluminum. The preceding analysis does not account for plastic flow near the crack tip.

The function $d(t)$, defined in Eqs. (26) and (27), assumes that the resulting displacement on A' after bonding can be written as the difference between the displacements in S^L, and in S^R before bonding. This is valid if the ratio of the Young's moduli of the materials is large, i.e., if one of the materials acts as a rigid body. Otherwise the resulting displacement on the interface must be considered an unknown function related to the material properties. In the experimental investigation conducted in this study, the modulus ratio was approximately 20; therefore Eq. (26) is a reasonable estimate of the resulting displacement on A'. An additional point with respect to the definition of $d(t)$ is that the displacement along the bond A' in S^L and S^R is assumed to be a linear function of position t. This assumption may not be quite accurate near the ends of the bond.

Finally, this analysis was conducted for two infinite half-spaces bonded along an arc A'. Comparison with finite-element results indicates that this theoretical solution agrees with the numerical solution at regions remote from the crack tip. Since it is difficult to accurately model high-stress-concentration areas in numerical analyses, no attempt was made at refining the initial analysis. Parametric studies of the relative dimensions of bond length to other specimen dimensions did not yield enough data to assess the effect of specimen geometry. Therefore, in applying the analysis in this study, data were considered acceptable only if the bond length was less than the other in-place dimensions of the specimen.

EXPERIMENTAL INVESTIGATION

Specimen Geometry and Loading

Experimental studies were undertaken to make quantitative measurements of the fracture parameter $\mathcal{J}$ for interfacial crack propagation. Based on the analysis of the preceding section, a specimen design was chosen and loading conditions were selected for which cracks would propagate at the interface between two dissimilar materials. Specimen design studies included photoelastic observations and strain-gage instrumentation of various specimens to determine how closely the theoretical analysis was satisfied. Aluminum-epoxy specimens were fabricated for a series of interfacial crack-propagation studies for various surface finishes on the aluminum-bonded interface. It should be noted that in the fabrication of bonded structures large residual stresses may arise. In the aluminum-epoxy specimen for this study, these stresses were due to restrained shrinkage along the bond during solidification of the epoxy and to differential thermal contraction during post-curing. The contribution of the residual field and the external loading to the energy required for interfacial crack propagation was computed using the analysis of the preceding section.

Aluminum plates 2 × 6 × 3/8 in. and 2 × 10 × 3/8 in. as shown in Fig. 6, were cleaned and etched as described in Appendix A. Epoxy plates 2 × 4 × 3/8 in. were cast against the aluminum and after initial curing were post-cured at 125°F for 4 hr. Before testing, a saw cut was made in each end of the epoxy along the interface with a 0.020-in.-thick blade. A razor blade was then used as a wedge to initiate a crack at the end of the sawed notch. Tensile or bending loads were then applied to the aluminum plates, and the progress of failure was observed. Under this loading cracks propagated along the interface, and if the bond length was small with respect to the plate dimensions, the data could be analyzed using the techniques presented in the previous chapter. These specimen geometries were satisfactory from the point of view of interfacial crack-growth

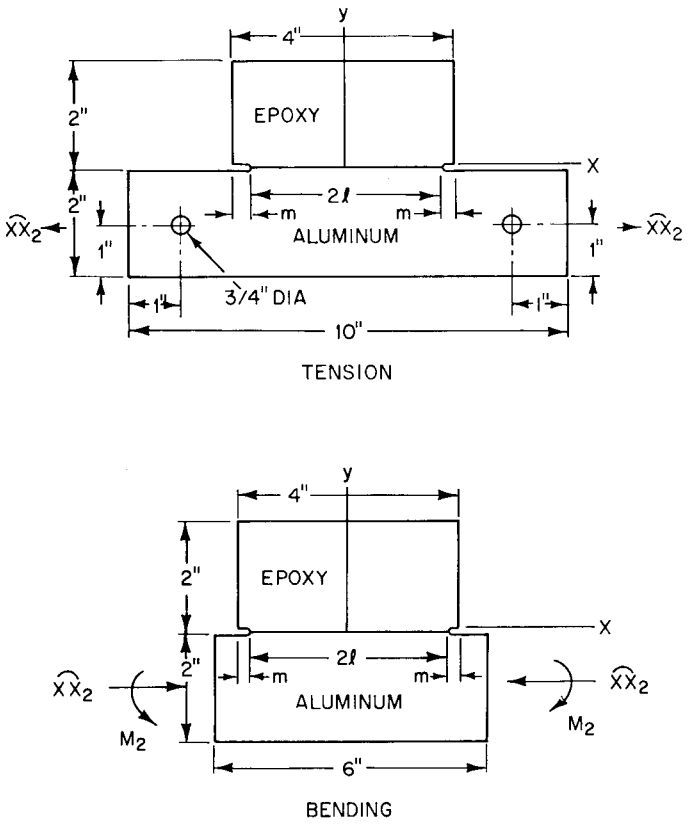

Fig. 6—Specimen geometries and loading conditions

observations. Furthermore, the specimens are amenable to photoelastic analysis and strain-gage instrumentation.

Before the actual crack-propagation studies were carried out, a photoelastic analysis was conducted (a) to determine the magnitude of the residual stress field's contribution to the energy required for interfacial crack propagation and also (b) to compare plane-stress and plane-strain theories developed in the previous section. Strain-gage studies verified the assumption of the strain field along the interface for tension and bending loading. These studies are described in the following sections.

Photoelastic Observations

As mentioned in the previous section, aluminum-epoxy plate specimens like those shown in Fig. 6 were loaded in tension, in bending, or thermally to produce interfacial crack propagation. Photographs and analysis of the light-field isochromatic fringe patterns are presented in this section for the tension and bending specimen, at progressively increasing loads, and for the thermal specimen at progressively decreasing temperature.

In addition to the bonded plate specimens, a specimen of somewhat different design was used for the compression studies. This specimen was made by taking an aluminum bar 1 X 1 X 6 in. and casting an epoxy block 2 X 4 X 3/8 in. with an epoxy surface 4 X 3/8 in. centrally placed on the 1- X 6-in. aluminum surface. The 1-in.-square bar was selected after numerous experimental studies indicated that buckling is a critical failure mode, rather than interfacial failure, for thinner specimens.

The compression studies were undertaken to determine the magnitude of the residual stress field induced due to casting and post-curing of the epoxy. Because of the difference in the coefficients of thermal expansion of these materials and the high curing temperature, a tensile stress resulted in the epoxy when the specimen was returned to room temperature. Applying a compressive load to the aluminum parallel to the bond would reduce the magnitude of the tensile residual stress. This reduction would be evidenced by a relaxation in the isochromatic pattern introduced during post-curing. Photographs of the light-field isochromatic fringe patterns for the compression study are shown in Fig. 7 (P = 47.1 lb). Initial birefringence, as in the first frame of Fig. 7, arose from two sources, elastic residual stresses and frozen stresses. The elastic stress field produced during the casting, post-curing, and subsequent cooling process stored elastic energy which was available for release to the fracture process. When the epoxy was debonded completely from the aluminum bar, birefringence due to the elastic stress field vanished, while birefringence due to the frozen stress field, which does not contribute to the fracture process, remained in the epoxy. To determine the magnitude of the elastic stress field, the positions of the isochromatic fringes were measured along the center line perpendicular to the bond for various compressive loads applied to the aluminum bar. These results are shown in Fig. 8. After crack-propagation tests were completed on tension and bending specimens, the epoxy was debonded, and the positions of the frozen isochromatic fringes were measured. From Fig. 8 the elastic strain required to produce an isochromatic pattern corresponding to the frozen isochromatic pattern was determined. As an example, the measurement of the position of the 1/2-order fringe taken from the frozen isochromatic patterns from 11 specimens ranged from 0.625 in. to 0.84 in. For these specimens the elastic strain due to residual stresses was 160 ± 30 μin./in. This value was used in calculations of the energy required for crack propagation along the bond.

The stress level required to extinguish the initial birefringence present in the epoxy was measured by observing the load at which the zero-order isochromatic fringe approached the bond. Zero-order extinction occurred at a compressive stress level of 8800 psi in the aluminum as determined from the isochromatic pattern at a load level of 8800 lb (184 X P), i.e., between values of 8600 lb (180 X P) and 9500 lb (200 X P) shown in Fig. 7. This result may be used to account for initial birefringence in comparing the isochromatic patterns observed with theoretical predictions of plane stress and plane strain.

As the loading increased, the appearance of the fringe pattern differed from those of the tension, bending, and thermal studies described later. The fringe order was no longer uniform along the bond, and the order of the fringes increased markedly as the crack tip was approached. For this specimen, crack propagation did not occur at the interface. Rather, the cracks deviated from the interface into the epoxy. This observation is in agreement with the theoretical analysis, which predicts compressive normal stresses near the crack tip that may inhibit interfacial crack propagation.

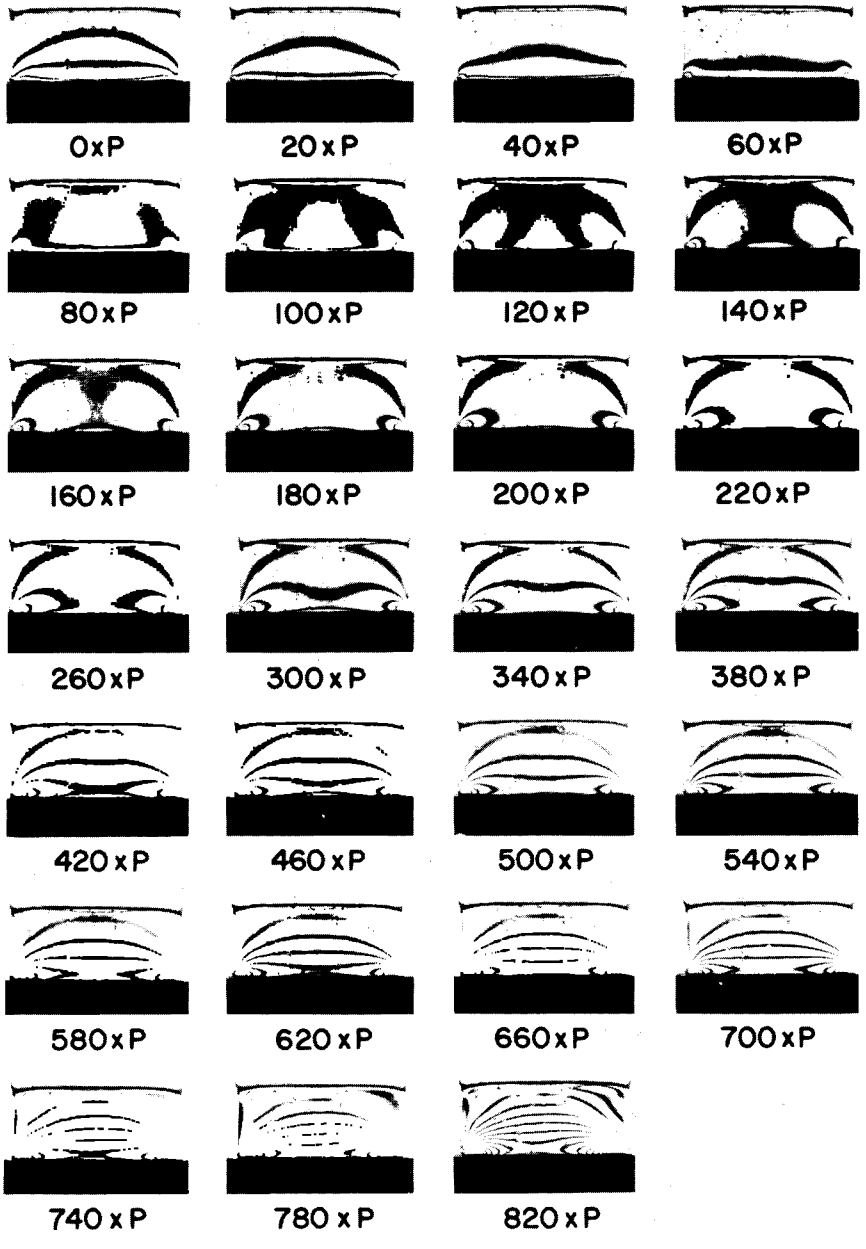

Fig. 7—Isochromatic patterns for a bonded plate under compressive loading; P = 47.1 lb

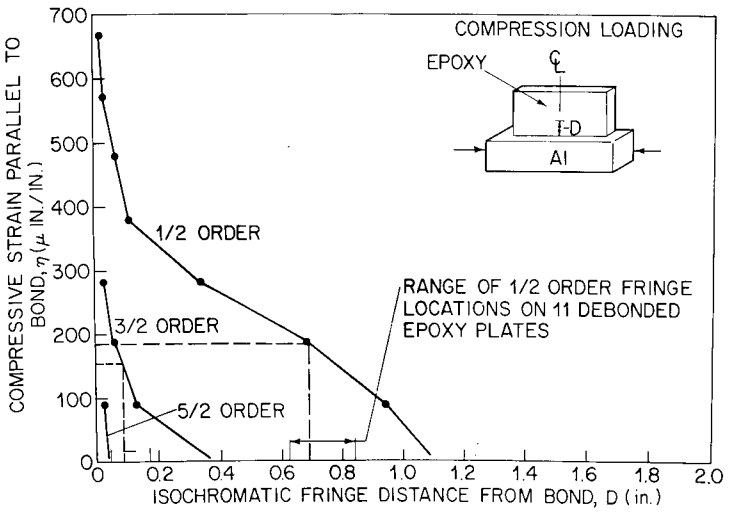

Fig. 8—Strain vs isochromatic fringe distance from bond under compression loading

Since they were subjected to the same post-cure cycle, the residual fringe patterns were similar in all of the specimens in this study. It should be noted that there was essentially no birefringent response before post-curing. After post-curing the fringe order was fairly constant along the length of the bond at approximately the 3-1/2 order. The fringes decreased in order from the interface to the edges of the epoxy plate.

For the tensile specimen, strain along the interface was determined from

$$\eta = \eta_M^L - \eta_M^R = \left(\frac{\widehat{xx}_1}{E_1} - \frac{\widehat{xx}_2}{E_2} \right) \tag{57}$$

where $\widehat{xx}_1$ and $\widehat{xx}_2$ are uniform stresses applied parallel to the bond in the epoxy and aluminum, respectively, and E_1 and E_2 are the Young's moduli of the epoxy and aluminum respectively. Using this expression, the strain along the bond was determined for the tensile specimen shown in Fig. 6. Isochromatic fringe patterns are shown in Fig. 9 for a tensile specimen under progressively increasing load (P = 18.8 lb). As shown in this figure, an increase in the load parallel to the bond resulted in an increase in the fringe order along the bond. Position of the fringes along the center line of the specimen vs strain determination, from Eq. (57), is shown in Fig. 10. From this data it was possible to estimate the fringe order at the interface along the center of the bond for various load levels. Extrapolating to zero load, the maximum shear-stress at the interface was found to be 480 psi. This agrees with the data in Fig. 9, which shows that the initial birefringence at the interface was slightly greater than the 3-1/2 order, which corresponds to a maximum shear stress of 465 psi. Theoretical values for the maximum shear stress at the center of the bond were computed for assumption of plane stress and plane strain and compared with the experimental values as shown in Fig. 11. Maximum shear-stress values were determined by forming the function $(\widehat{xx}_1 - \widehat{yy}_1)/2$ at the center of the bond from the real part of Eq. (40) evaluated at t = 0 and from the following expression for $\widehat{xx}_1$ [8]:

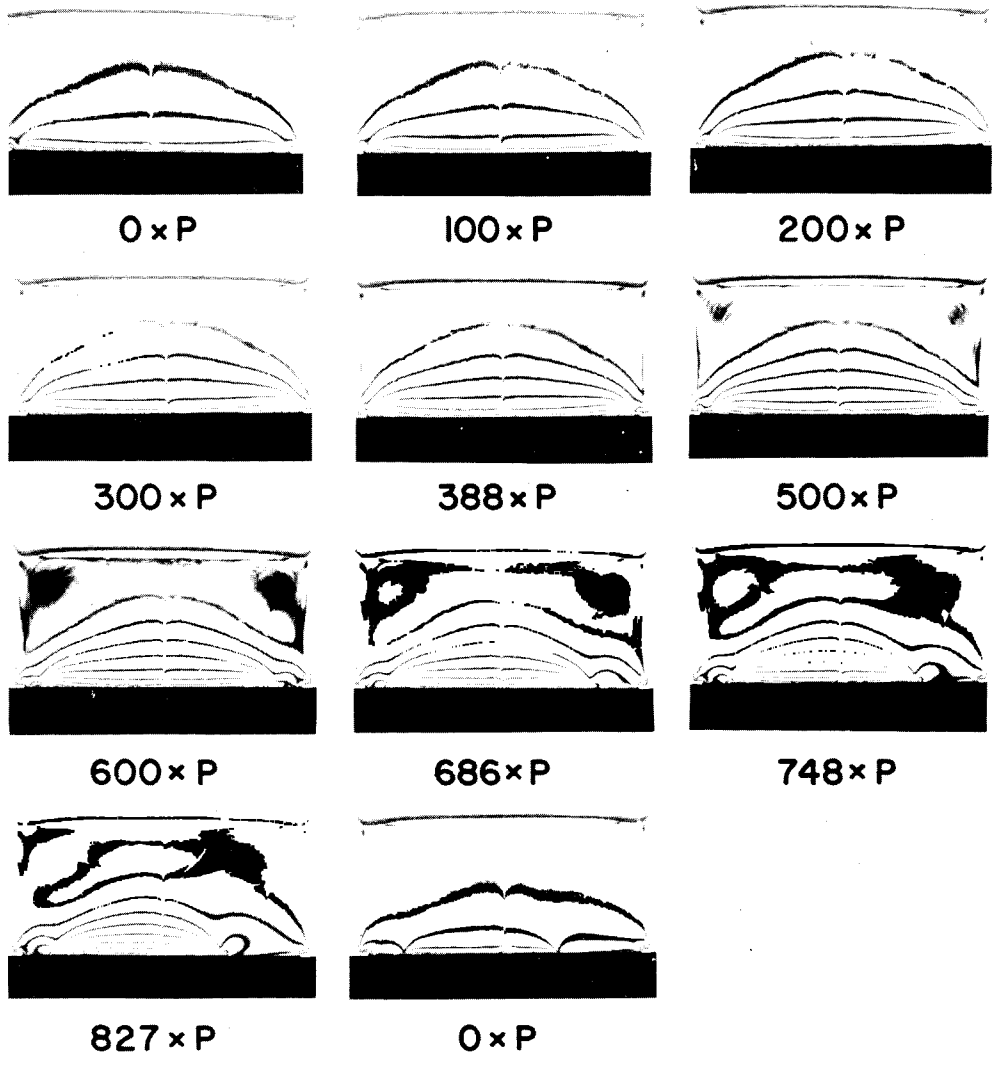

Fig. 9—Isochromatic patterns for a bonded plate under tensile loading; P = 18.8 lb

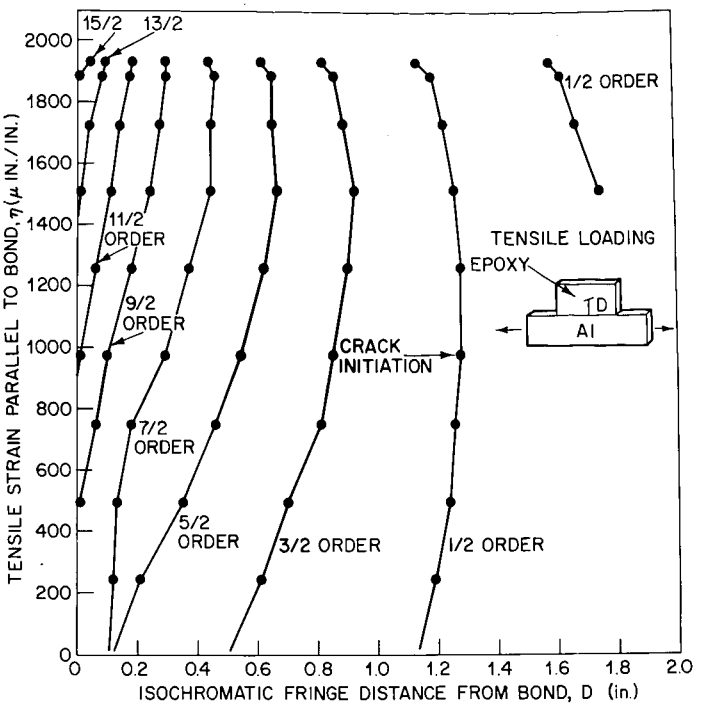

Fig. 10—Strain vs isochromatic fringe distance from bond under tensile loading

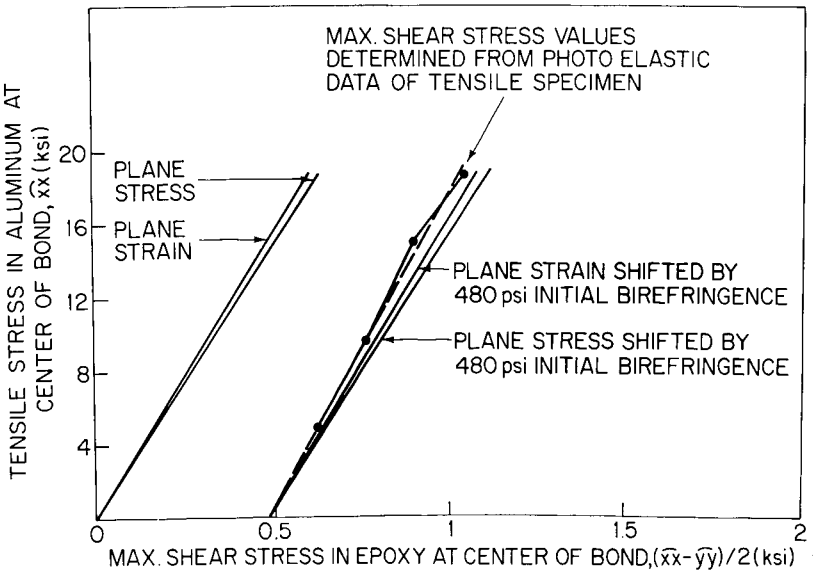

Fig. 11—Comparison of theoretical shear stress with experimental values for plane stress and plane strain

$$\widehat{xx}_1 = \frac{\frac{\aleph_2 + 1}{\mu_2}}{\frac{\aleph_2 + 1}{\mu_1}} \widehat{xx}_2 . \tag{58}$$

Although there is little difference between plane-stress and plane-strain assumptions for these materials, the plane-strain analysis approximates the experimental data more closely than does plane stress, and this method was used in the subsequent analyses.

As shown in Fig. 9, the fringe order at the interface increased as the load was applied, up to approximately the 6th order, at which time the cracks began to propagate at the interface. It was relatively easy to follow the progress of the cracks, since the fringes approach the interface near the crack tip. As the crack propagated, the fringe order along the bond remained approximately constant, increasing from the 6th order at 7330 lb (388 × P) to the 8th order at 14,200 lb (748 × P). Crack initiation occurred at 7330 lb which corresponds to a strain of 1020 μin./in. along the bond. To determine the total strain for crack initiation, this value must be added to the 160 μin./in. of strain due to the residual field. For the specimen shown in Fig. 9, the residual field contributes approximately 15% of the strain required for crack initiation.

Bending was applied to specimens shown in the lower portion of Fig. 6, using the loading fixture in Fig. 12. This loading fixture transmits compressive loads as well as bending loads, which result in tensile strain along the bond. Typical results for these studies are shown in Fig. 13 and 14. The slight striation evident in Fig. 13 is due to nonuniformities in the epoxy along the bond. For this specimen, the strain along the interface due to bending was determined from

$$\eta = \eta_M^L - \eta_M^R = -\frac{y^L}{R^L} + \frac{y^R}{R^R} \tag{59}$$

where, as shown in Fig. 15, $y^L = y - h_e/2$ is the height of the neutral axis of the epoxy plate of depth h_e above the bond, $y^R = y + h_a/2$ is the height of the neutral axis of the aluminum plate of depth h_a below the bond, and R^L, R^R are the radii of curvature of the neutral axes of the epoxy and aluminum, respectively.

This geometric description for bending analysis of two bonded plates follows closely the methods used by Boley and Weiner [29] for thermoelastic analysis of bending and buckling of bimetallic beams. Evaluating this expression on A' corresponds to setting $y = O$ in the relations for y^L and y^R defined above. It is interesting to note in Fig. 14 that a variation occurs in the 1/2-order fringe at the onset of crack growth. In the previous tensile data this variation was not so pronounced, and the tensile field did not extend as far into the epoxy as in the bending case. In the Fig. 13 specimen, as in the previous case, crack propagation was not symmetric along the bond.

Although only limited data were obtained for the thermal studies (Fig. 16 and 17), these fringe patterns were similar to those for tension or bending loading. In the thermal loading studies, the temperature gradient was maintained at approximately 4°F/hr to ensure thermal equilibrium. Attempts to decrease the temperature at higher rates produced

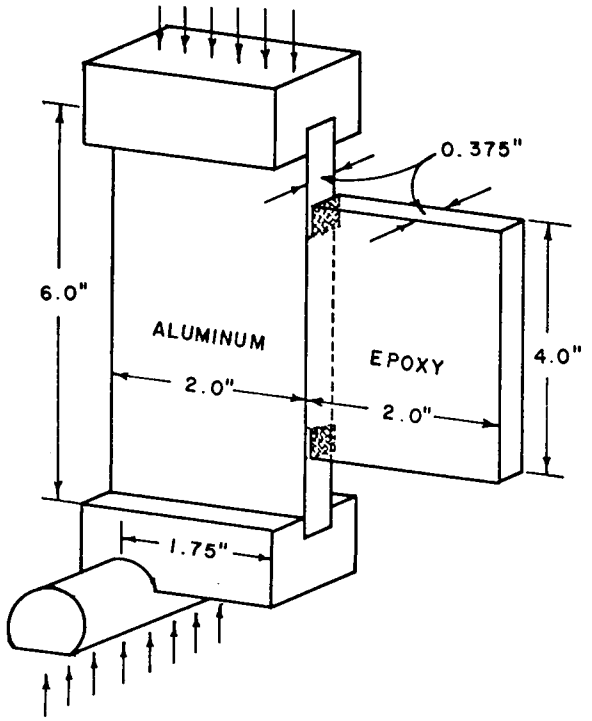

Fig. 12—Specimen geometry and loading fixture for bending loading

extensive cracking in the epoxy due to thermal gradients. Strain along the interface was determined from

$$\eta = \eta_T^L - \eta_T^R = (\alpha_1 - \alpha_2)(T_I - T_F), \tag{60}$$

where α_1 and α_2 are the coefficients of thermal expansion of the epoxy and aluminum, respectively, and $T_I - T_F$ is the difference between initial temperature and final temperature.

Instrumented Specimen

The theoretical analysis discussed in the preceding chapter was for two infinite elastic half-spaces bonded along A'. However, for the finite specimen geometry selected for this study, it was necessary to determine how closely the applied loading satisfied the assumed strain field at the interface. In order to determine the strain distribution in these specimens, a tension sample, a bending sample, and a compressively loaded bar were instrumented with strain gages. The tension specimen had six foil gages bonded to the aluminum bar, as shown in Fig. 18. The bending specimen (Fig. 19) had six gages mounted in the same locations as on the tension specimen. In addition a gage was mounted on the opposite side of the aluminum plate in the center to determine bending through the thickness. Use of data from these specimens resulted in redesigned loading grips, which minimize out-of-plane bending and ensure a uniform stress field (Fig. 12). A compressively loaded

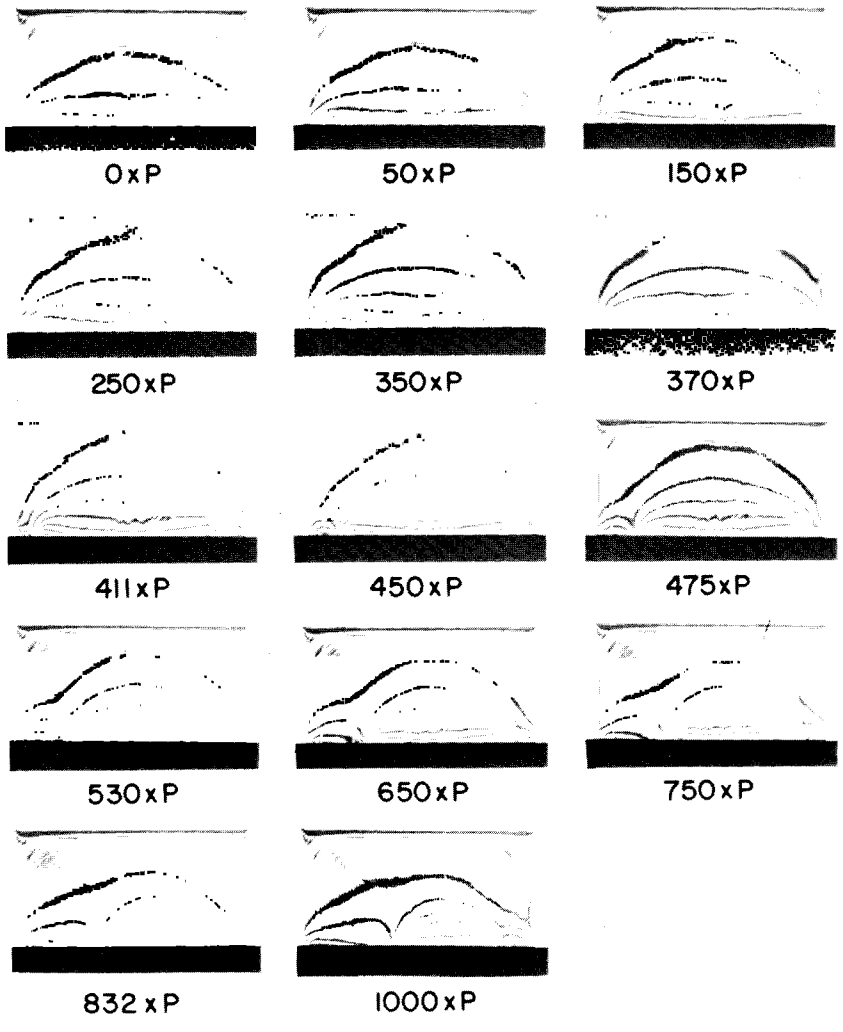

Fig. 13—Isochromatic patterns for a bonded plate under bending loading; P = 9.4 lb

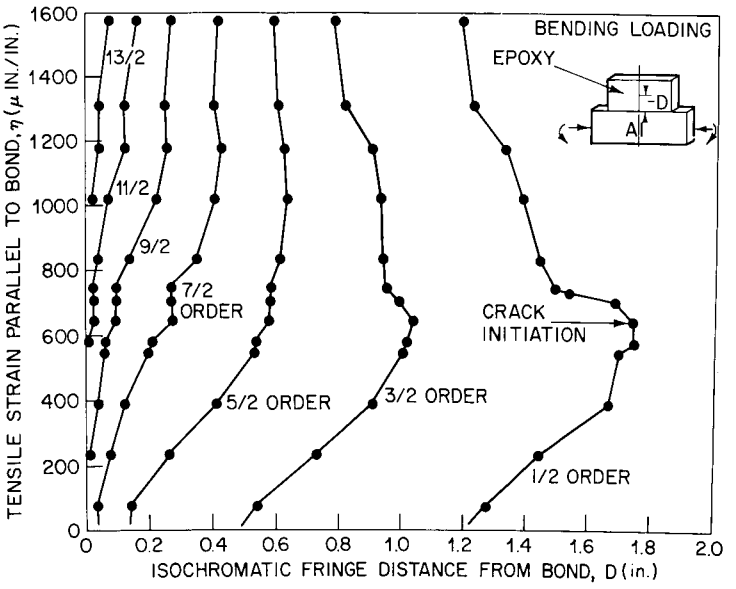

Fig. 14—Strain vs isochromatic fringe distance from bond under bending loading

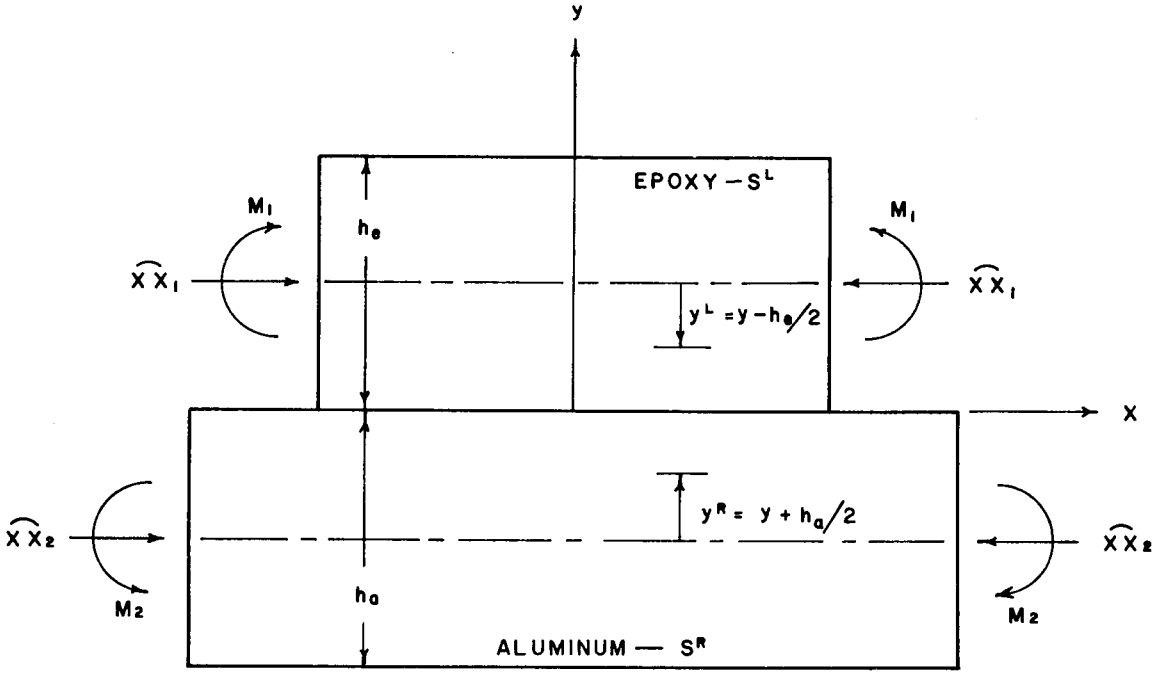

Fig. 15—Plate specimen under self-equilibrating bending and compression loading

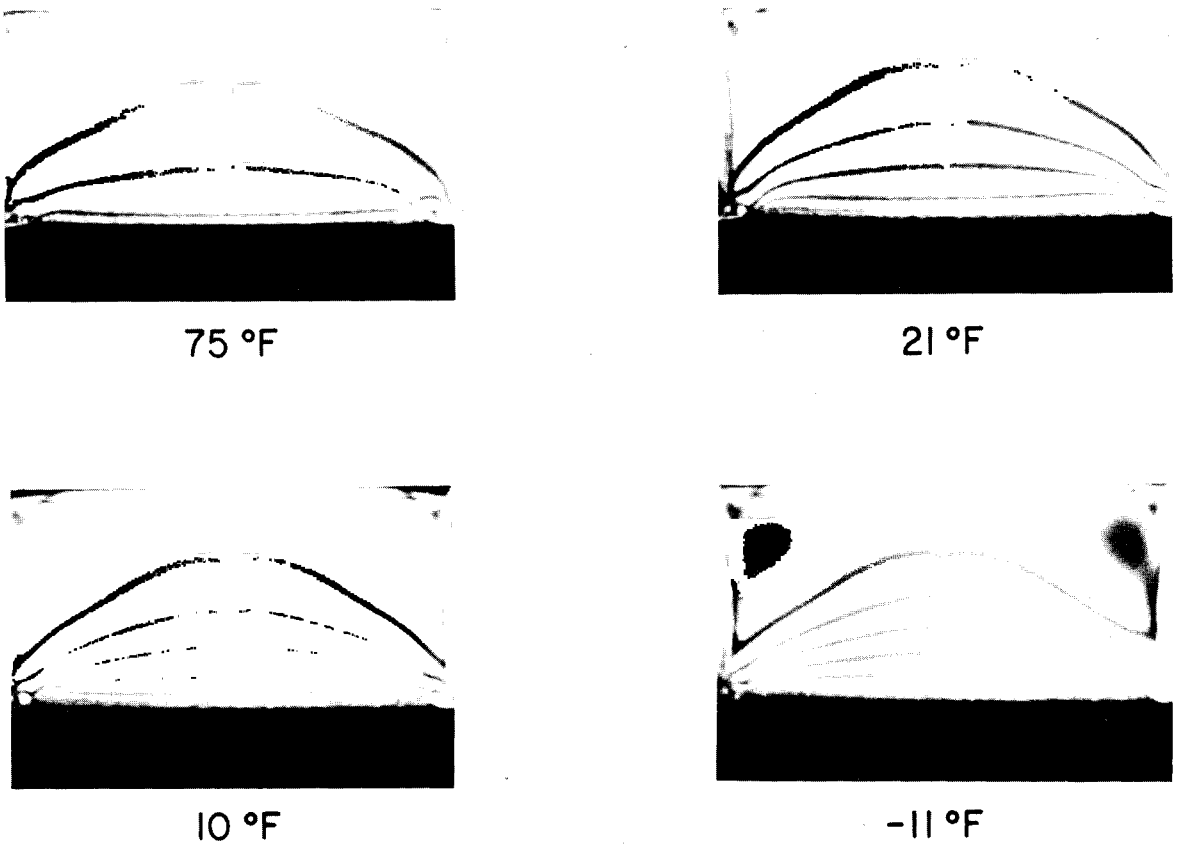

Fig. 16—Isochromatic patterns for a bonded plate under thermal bending loading

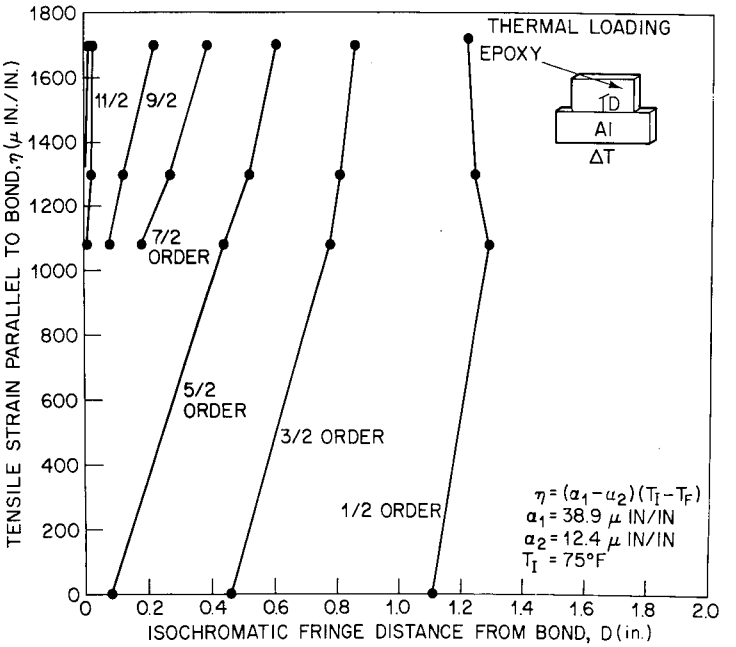

Fig. 17—Strain vs isochromatic fringe distance from bond under thermal loading

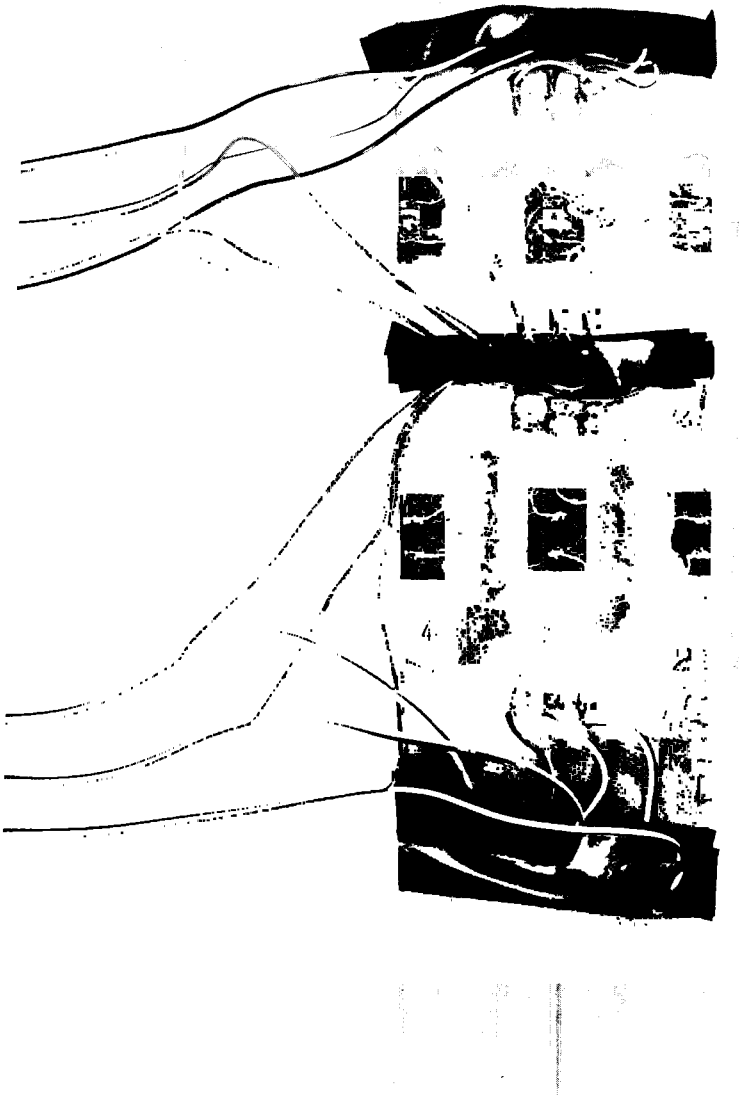

Fig. 18—Strain-gage locations for a tension specimen

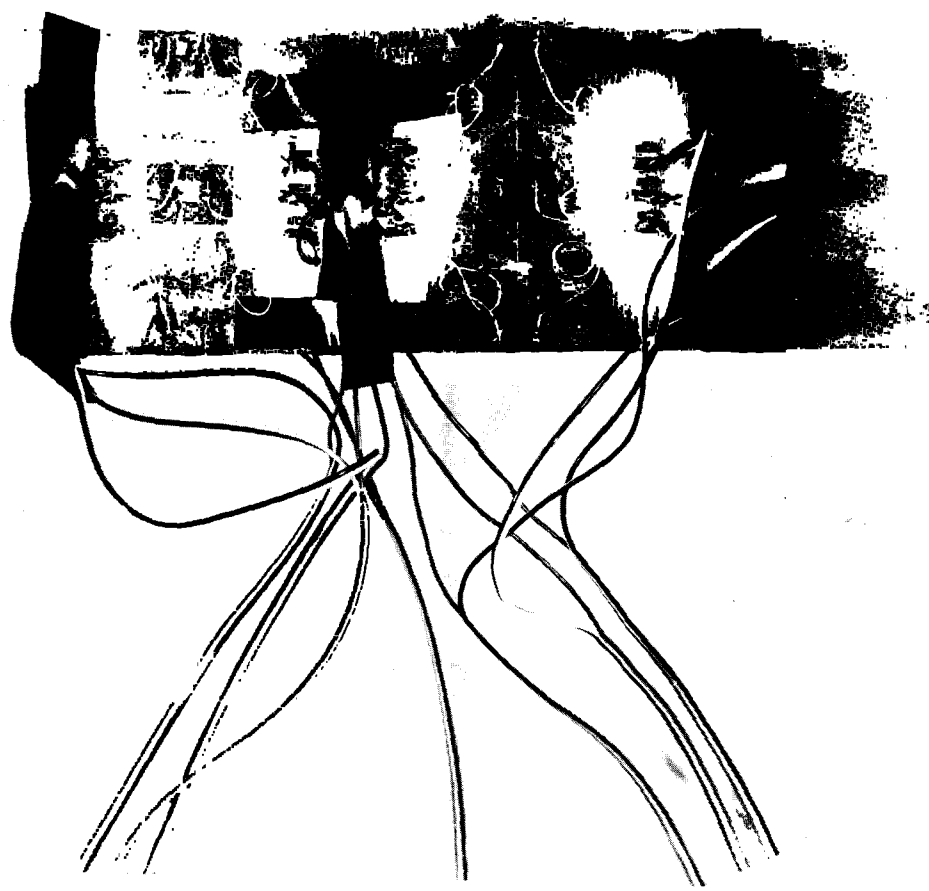

Fig. 19—Strain-gage locations for a bending specimen

specimen, as shown in Fig. 20, was instrumented with a "Flexagage,"* which is composed of two gages separated by a 0.040-in.-thick laminated strip. With this transducer, it was possible to separate the bending and axial load components for the compression specimen.

Results of the tensile studies for the six gages, shown in Fig. 21, indicate close agreement with the strain field computed for uniform loading. The maximum observed deviation from these data was approximately 7%. Load-strain profiles are shown for the bending specimen in Fig. 22 and 23. Although greater variation was observed in these data, these results are also in good agreement with the computed strain field. The small differences in strain recorded by gages 1 and 3 and shown in Fig. 23 indicate a negligible amount of out-of-plane bending. In both of these specimens, it is important to note that little variation occurred between the two gages along the bond. The results of the compression studies, shown in Fig. 24, indicate that plastic deformation occurs in the bar for loads above 35,000 lb. It is at this level that crack propagation occurred in the compression sample, and thus deviations are observed from the stress field predicted by the linear elastic analysis.

Crack-Propagation Studies

A series of aluminum-epoxy specimens was prepared to evaluate the effects of surface finish of the aluminum on the strain-energy release rate. These surfaces were chosen to represent the range of surface finishes in actual bonding applications. Detailed discussions of the surface finishes and specimen preparation are presented in Appendix A. Surface-roughness measurements were made with a profilometer to characterize the various surface finishes on the aluminum. Specimens were mounted in a closed-loop servocontrol testing machine, and loading was applied at a rate of approximately 500 lb/min. A scale was attached to the side of each specimen, and photographs were taken at various intervals of crack length. In addition, indications of crack length were made on the sides of the specimen with a marker. To determine the strain energy release rate from the formulation in the preceding section (Eq. (56), the load at each interval of crack length was required in addition to the material properties. Details of this analysis are presented in the next section for various surface finishes and types of loading. As discussed in the section on photoelastic studies, photoelastic data from the tension and bending tests were used to determine the contribution of the residual field to the energy required for crack propagation. For some polymers, the strain-energy release rate is dependent on the crack velocity. Therefore, measurements were made of the time interval between crack-length recordings. Estimates of the range of crack velocities were computed from these data.

The epoxy and aluminum fracture surfaces were examined by both optical techniques and scanning electron microscopy. These studies were undertaken to determine whether the crack propagates in the epoxy near the interface or at the interface itself, how the various surface finishes affect the path of the crack, and what correlation can be observed between the appearance of the failure surface and the measured values of strain-energy release rate.

*Budd Instrument Company.

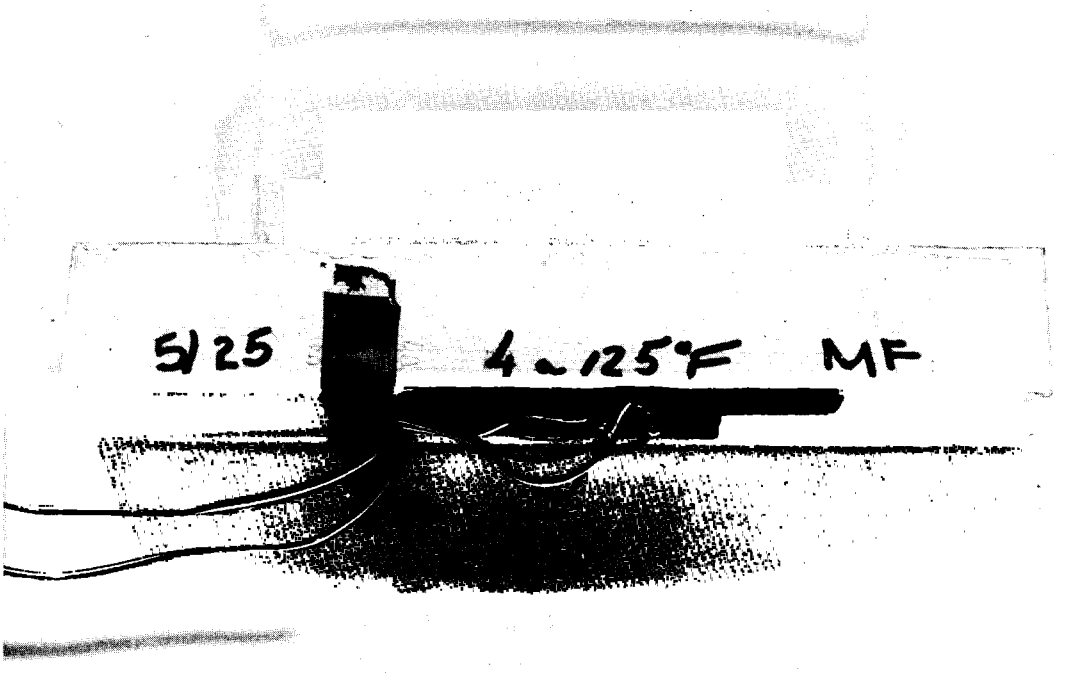

Fig. 20—Strain-gage locations for a compression specimen

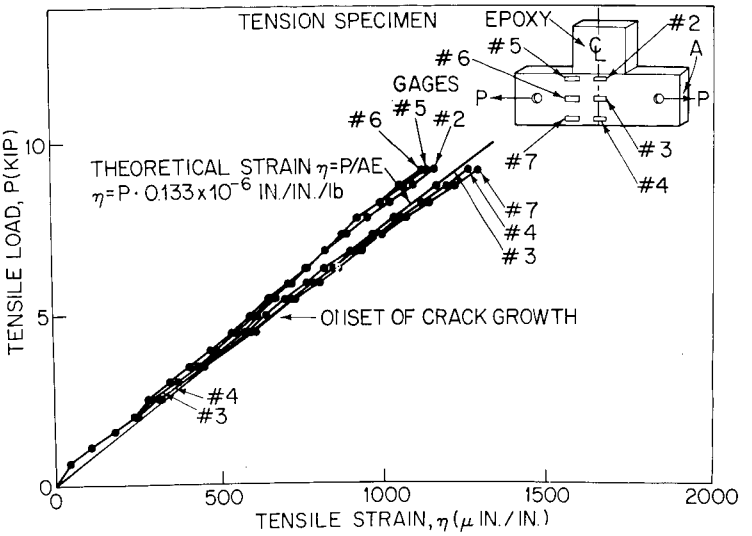

Fig. 21—Load vs tensile strain for a tension specimen

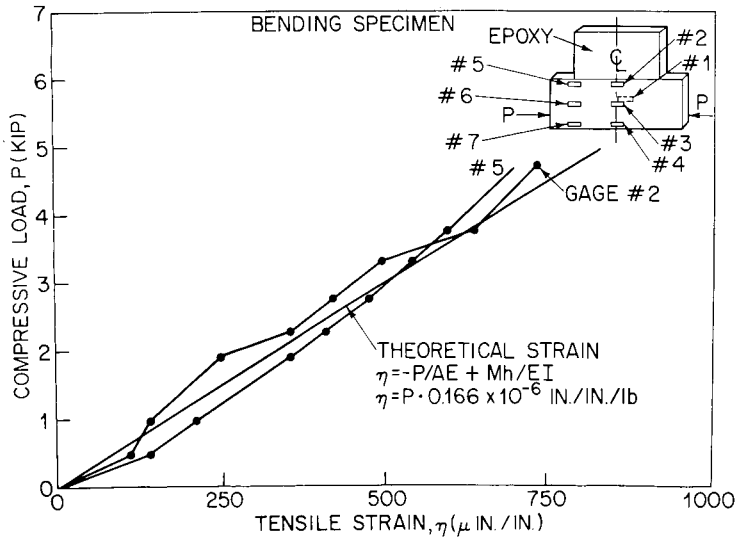

Fig. 22—Load vs tensile strain for a bending specimen

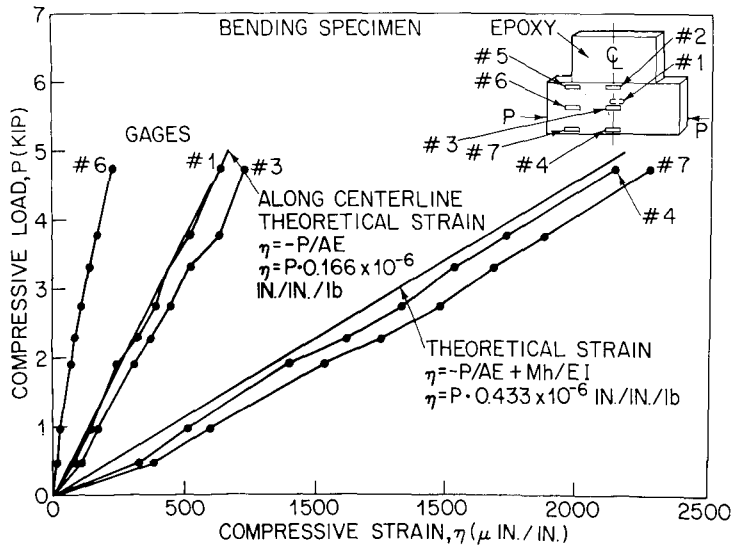

Fig. 23—Load vs compressive strain for a bending specimen

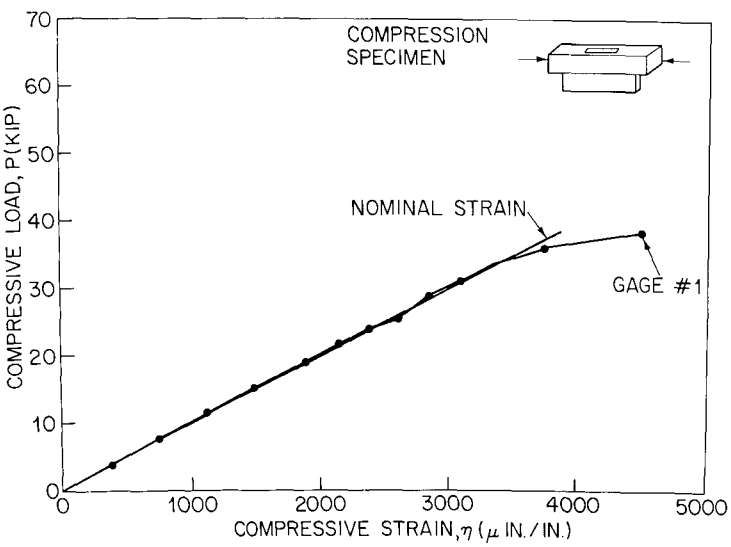

Fig. 24—Load vs compressive strain for a compression specimen

RESULTS AND DISCUSSION

Results of Crack-Propagation Studies

With the formulation developed in the theoretical analysis, the strain-energy release rate $\mathcal{G}$ was calculated at various crack lengths along the bond. It should be noted that this analysis is for two-dimensional bonded plates under either plane-stress or plane-strain conditions. In general, analysis of bonded plates should be considered as a three-dimensional problem, since these plates experience a contraction in thickness during curing or under mechanical loading. Durelli, et al. [30], have shown that this pinching has little effect on the normal stress and strain along a bond for materials with a Poisson's ratio of $\nu = 0.3$, and consequently the two-dimensional analysis was considered adequate. As discussed previously, plane-strain conditions were assumed in this analysis. From a physical point of view this is a reasonable assumption, since the aluminum constrains the epoxy at the interface. At regions remote from the interface, plane-stress analysis may be more appropriate, since this constraint is no longer present.

Values of $\mathcal{G}$ were computed for crack-length to initial-bond-length ratios equal to or greater than 0.5. Under these conditions the infinite-plate assumption closely approximated, since the bond length is less than the plate height or width.

Data shown in Fig. 25 are for four specimens, the aluminum surfaces of which were glass-peened and etched before bonding. For all loading conditions, $\mathcal{G}$ increased initially and then approached a constant value, although some specimens exhibited considerable variation. Unloading and subsequent reloading caused crack growth to begin at lower toughness levels.

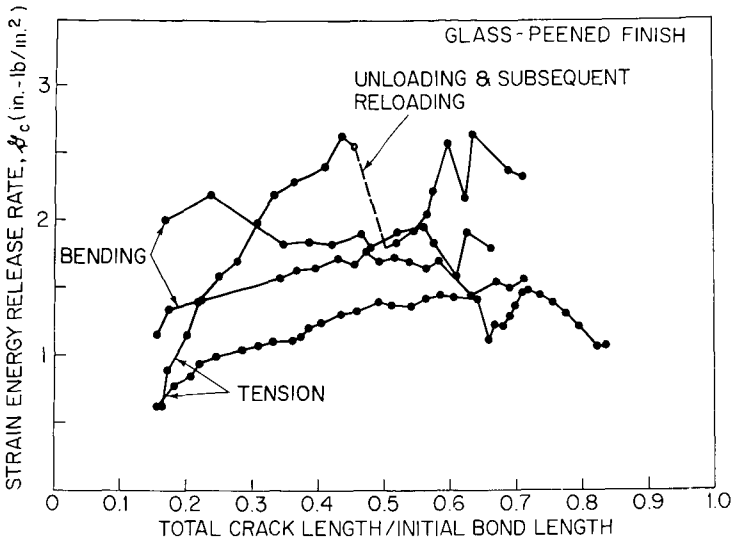

Fig. 25--Strain-energy release rate vs crack length/initial bond length for glass-peened surfaces

Similar data are shown in Fig. 26 for five specimens with milled and etched aluminum surfaces. Again the $\mathcal{G}$ values increased initially and then approached relatively constant values.

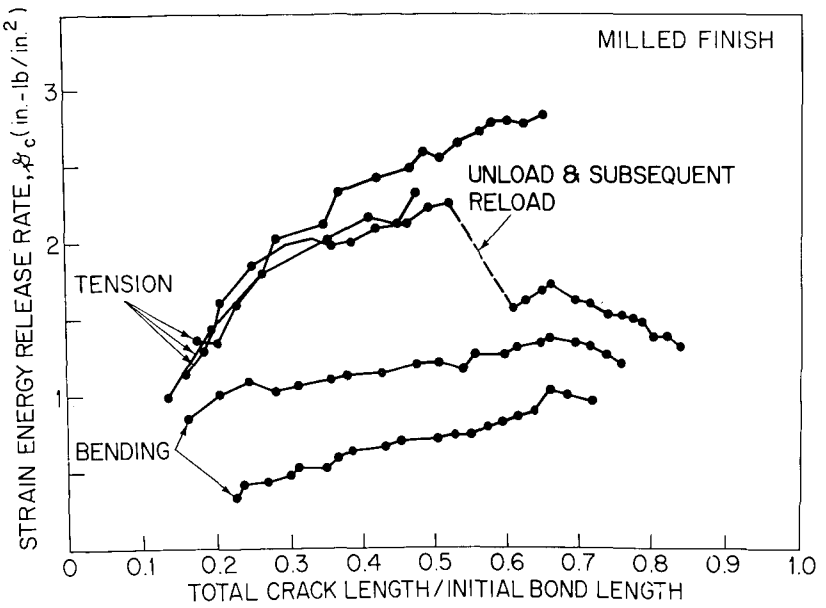

Fig. 26—Strain-energy release rate vs crack length/initial bond length for milled surfaces

As before, unloading and reloading caused crack initiation at lower toughness levels. In this case $\mathcal{G}$ did not return to its former level. These values of $\mathcal{G}$ did not differ appreciably from those for glass-peened surfaces. For both glass-peened and milled surfaces, crack propagation at the interface was stable. Crack stability here implies that under constant load conditions the crack did not accelerate and cause catastrophic failure of the specimen. Thus, when the load was maintained at a constant level, the crack stopped. Under these conditions delayed crack growth may take place because of creep or material degradation, but that kind of failure was not explored in this study.

Data shown in Fig. 27 are for four specimens with sandblasted and etched aluminum surfaces. Here $\mathcal{G}$ was greater initially than for the glass-peened or milled specimens and increased as the crack propagated. It was possible to extend the crack only slightly beyond the point at which the ratio of crack length to initial bond length was 0.5, due to constraints in the loading system. For these specimens, the strain-energy release rate values are greater than for the milled or glass-peened surfaces. In some cases cracks jumped in small increments near the interface, although more remote from the bond than for stable propagation. This indicates a possible change in the mode of failure, which may be related to surface roughness, rate of loading, or both.

Data shown in Fig. 28 compare the results for bending tests on glass-peened, milled, and sandblasted surfaces with results for polished aluminum surfaces. These values are generally greater than the value of $\mathcal{G}_c$= 0.5 in.-lb/in.^{2} reported by Mostovoy and Ripling [31] for the bulk epoxy system. However, for the polished specimens, the value of $\mathcal{G}$ is approximately equal to the bulk value. This result implies that for opening mode failure studies, such as those conducted by Mostovoy and Ripling, either cohesive or interfacial failure may occur if the adherends are polished, whereas interfacial failure will not occur if the adherend surfaces are milled, glass-peened, or sandblasted. Results have shown that environmental effects may weaken the interface, but that topic was not treated in this study.

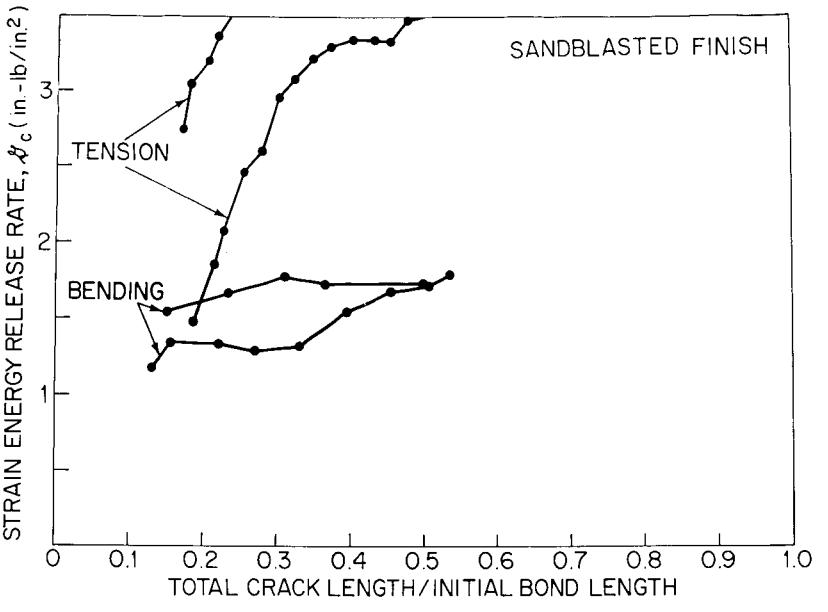

Fig. 27—Strain-energy release rate vs crack length/initial bond length for sandblasted surfaces

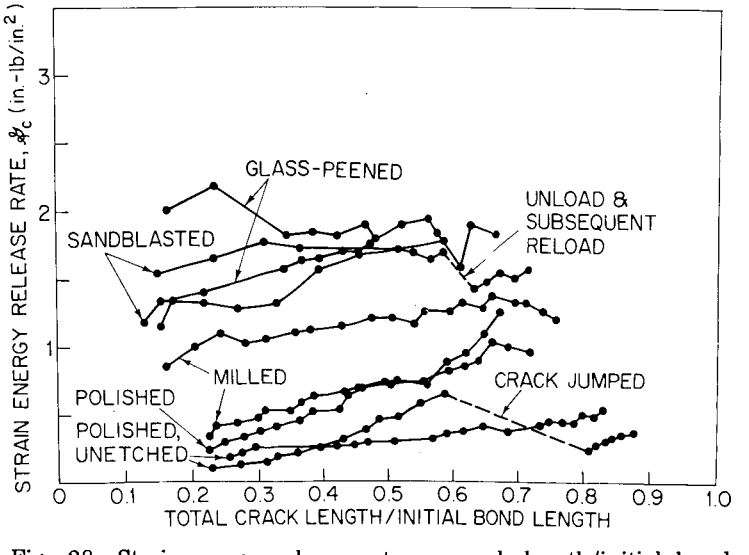

Fig. 28—Strain-energy release rate vs crack length/initial bond length for specimens with various surface finishes under bending loading

A summary of the average strain-energy release rates and crack velocities is presented in Table 1. Polished, milled, glass-peened, and sandblasted surfaces were etched before casting of the epoxy, except as noted. Included also are measured values of the surface roughness for the various surface finishes in both etched and unetched conditions. Surface-roughness measurements were made with a profilometer that draws a tracer point across the surface and indicates the arithmetic average of the roughness. The tracer point used for these measurements was conical and had a hemispherical tip with a 0.0005-in. radius. Figure 29 shows that for polished, glass-peened, and sandblasted surfaces etched prior to casting and subjected to bending loading, there is a linear relation between surface roughness and strain-energy release rate. This can be expressed as

$$\mathcal{G} = 0.014S + 0.9 \tag{61}$$

where S is the surface roughness in microinches. Data in Table 1 indicate that the roughness of the milled surface is nonuniform, i.e., the surface roughness along the length of the bond is greater than the roughness in the thickness direction. From fracture-surface observations it is apparent that this variation is due to the milling operation, which produces high roughness values in the longitudinal or lengthwise direction but low values in the thickness direction. Roughness measurements in the thickness direction of the milled specimens fall within the range predicted from the relation between surface roughness and strain energy release rate for the other surface finishes studied. Therefore, the strain energy release rate may be determined from the minimum value of surface roughness over the range considered in this study.

Scatter in the data may be due to variations in material properties of the epoxy. As described in Appendix A, the epoxy resin is heated to 110°F before casting to remove entrapped air and decrease viscosity. An amine hardener was then added to the epoxy resin at 110°F. Because of the short "pot life" of this epoxy system, only three

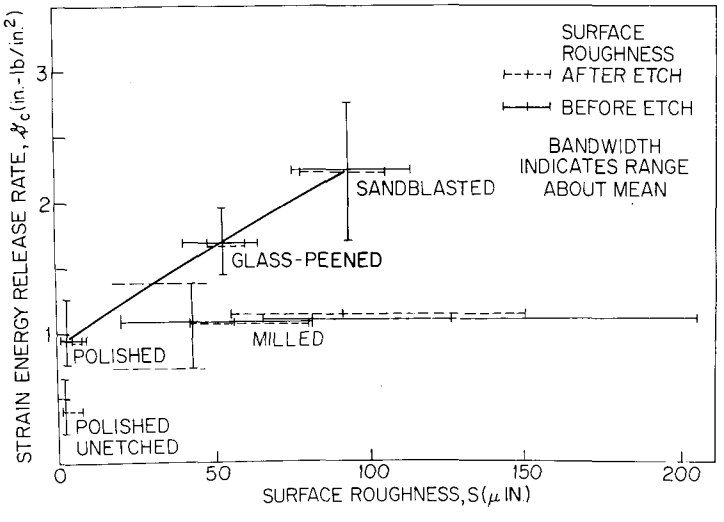

Fig. 29—Strain-energy release rate vs surface roughness for specimens under bending loading

Table 1
Average Strain Energy Release Rates, Crack Velocities, and Surface Roughness Measurements

Test and Surface Condition	Spec	Polished (Unetched)		Polished		Milled		Glass-Peened		Sandblasted	
		$\bar{X}$*	S†	$\bar{X}$	S	$\bar{X}$	S	$\bar{X}$	S	$\bar{X}$	S
Tension											
$\mathcal{G}$ in.-lb/in.^{2}	1	—‡	—‡	—‡	—‡	1.6	0.22	1.3	0.13	3.6	0.06
	2	—‡	—‡	—‡	—‡	2.7	0.10	2.2	0.30	—‡	—‡
$\dot{m} \times 10^{-3}$in./s	1	—‡	—‡	—‡	—‡	1.5	—‖	2.4	—‖	1.3	—‖
	2	—‡	—‡	—‡	—‡	1.2	—‖	1.1	—‖	—‡	—‡
Bending											
$\mathcal{G}$ in.-lb/in.^{2}	1	0.40	0.15	1.0	0.20	0.8	0.11	1.6	0.10	2.5	0.44
	2	0.42	0.07	—‡	—‡	1.3	0.06	1.9	0.13	1.8	—‖
$\dot{m} \times 10^{-3}$in./s	1	3.2	—‖	3.6	—‖	3.2	—‖	—‖	—‖	—‖	—‖
	2	3.3	—‖	—‡	—‡	—‖	—‖	—‖	—‖	—‖	—‖
Surface Roughness											
Unetched	L¶	2.4	1.1			126	32.9	53	4.8	93	8.1
	T**					43	14.6				
Etched	L			6.6	1.1	91	26.8	51	3.6	92	7.4
	T					56	11.4				

*Average value.
†Standard deviation.
¶ L = Longitundinal or lengthwise direction.
**T = Transverse or thickness direction.
‡No test
‖Insufficient data

specimens could be cast from a single mixture. Even under these conditions, slight discoloration and striation occurred in some of the specimens, indicating nonhomogeneous mixing or curing. Scatter in the data runs also due to unloading and subsequent reloading, which produced variations in $\mathcal{G}$ with crack length.

Fracture-Surface Observations

Indications from optical observations of the fracture surfaces at 30X (Fig. 30) show that the crack replicates the surface finish of the aluminum as it propagates along the bond. Based on the relation developed between initial surface roughness and $\mathcal{G}$, greater roughness of fracture surfaces in the epoxy indicate that strain-energy release rates were required for crack propagation. The effect of loading rate or crack velocity on this behavior was not considered here, although this is an important factor that may affect the failure mode. This result is useful in analyzing failures of bonded structures. In many instances the circumstances that caused failure are unknown, and the origin, direction of crack propagation, and energy required for crack growth must be determined from observations of the failure surface.

Studies made at higher magnification, using the scanning electron microscope (Fig. 31) indicate that a residue of epoxy remains bonded to the aluminum surface. These studies also indicate that for stable crack propagation, crack growth occurs very near the interface. Studies conducted by Bascom [32] on scarf joints of aluminum bonded with epoxy also indicate that a residue of epoxy remains on the aluminum after interfacial failure. By radioisotope tagging with Carbon-14, he found that a 300- to 500-*A* layer of resin is left on the aluminum. His fractured specimens also exhibit replication of the scratches and machining marks of the aluminum surface on the resin fracture surface.

SUMMARY AND CONCLUSIONS

The purpose of this investigation was to characterize crack propagation at the interface between two dissimilar materials, using a formulation based on strain-energy release rate, and to determine the contribution of the residual stress field to the energy required for crack propagation at an epoxy-aluminum interface. To this end, a theoretical analysis was developed for the plane problem of two elastic half-spaces in contact along an arc. The stress analysis included the previously solved cases for thermal and tensile loads and included a new formulation for bending loads. In summary, the stress analysis predicted that (a) compressive normal stresses should occur near the crack tip when compressive loads are applied to the aluminum parallel to the bond, or bending loads, which result in compressive stresses in the aluminum parallel to the bond; these conditions inhibit interfacial crack growth. The analysis also predicted that (b) tensile normal stresses should occur near the crack tip when tensile loads are applied to the aluminum parallel to the bond, or bending loads, which result in tensile stresses in the aluminum parallel to the bond; these conditions are necessary for interfacial crack propagation. Thirdly, the analysis predicted that (c) tensile normal stresses should occur near the crack tip under thermal loading when the temperature is reduced below the postcuring temperature; under these conditions interfacial crack propagation occurs when the thermal gradient is

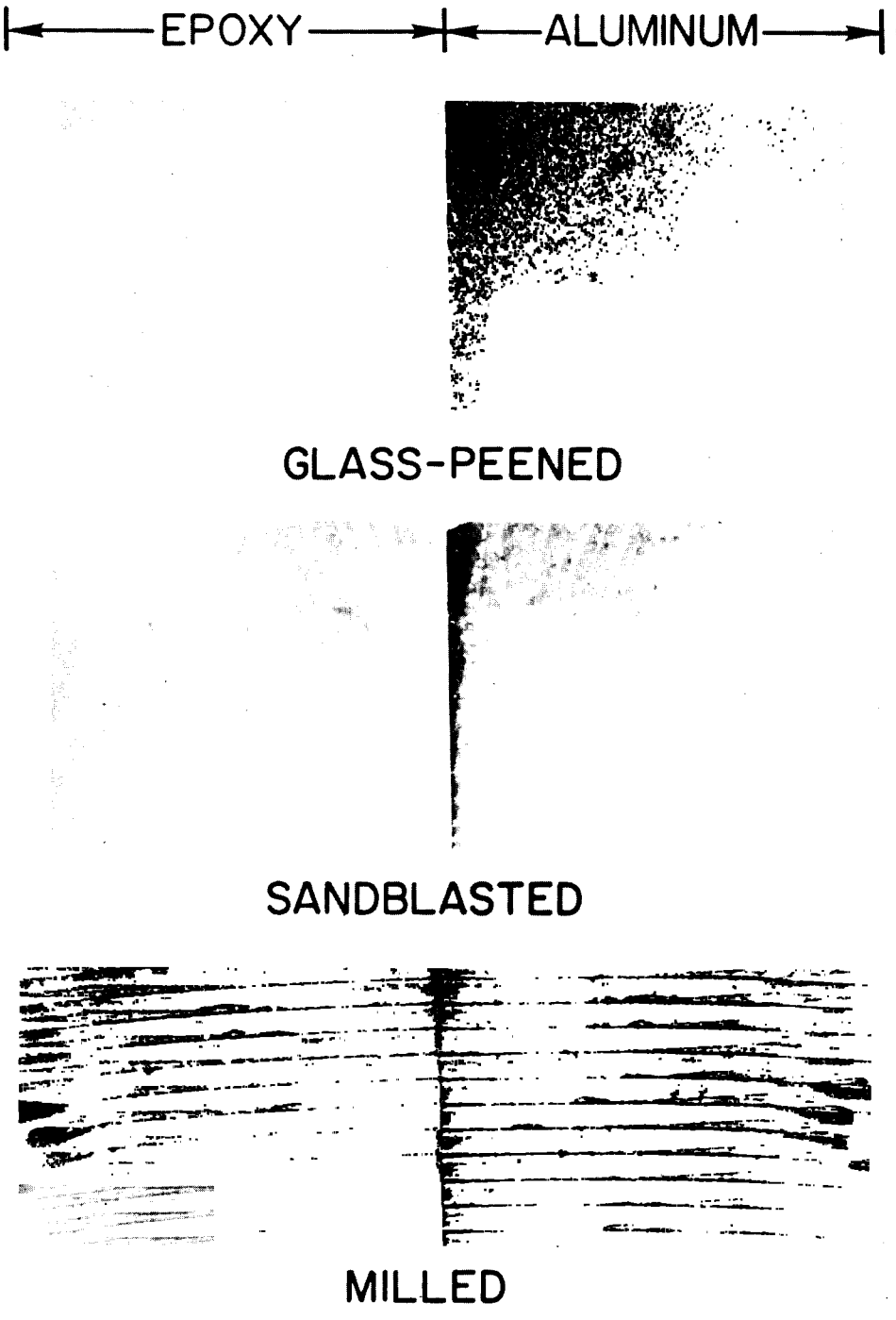

Fig. 30—Fracture surfaces of epoxy—aluminum specimens with three surface finishes; 30X magnification

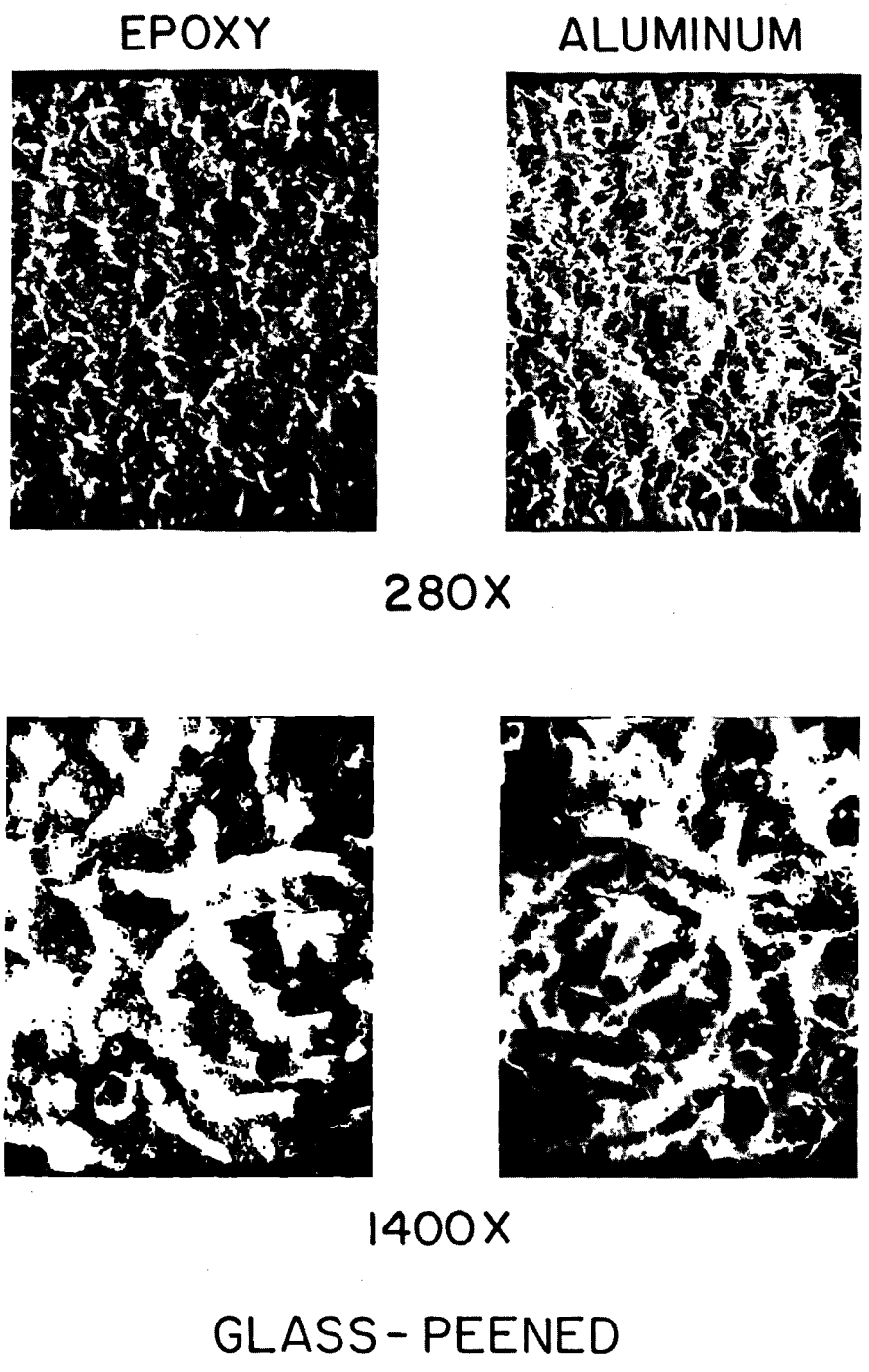

Fig. 31—Scanning electron microscope photographs of glass-peened epoxy—aluminum fracture surface

low. Rapid temperature reduction, however, causes complete cracking of the epoxy even at regions remote from the interface. As described in Appendix A, good agreement was obtained between the theoretical analysis and a numerical analysis of the stress distribution in the specimen geometry chosen for this study.

From the stress analysis a fracture-mechanics formulation was developed to describe interfacial failure. Experimental studies described below demonstrated that this formulation could be used to analyze crack propagation along the bond for aluminum-epoxy specimens under tensile, bending, or thermal loading. It was not possible to propagate cracks along the bond under compression loads, since the cracks deviated from the bond and propagated into the epoxy. As summarized above, under compression loading the stress field determined by the theoretical analysis predicted that compressive normal stresses were present in the vicinity of the crack tip. These stresses prevent interfacial failure, and other failure modes must be considered, depending on the relative toughness of the two materials and the direction of the maximum tensile stress.

Various specimen configurations were examined during the course of this study, viz, an epoxy strip bonded to an aluminum beam loaded in flexure, an epoxy annulus bonded to an aluminum rod loaded in tension, and an epoxy plate bonded to an aluminum plate loaded in tension or bending. While there were advantages to each of these specimen geometries, the bonded-plate specimen was chosen because of ease of fabrication and testing and because an analysis was available to describe the stress state and to formulate the strain-energy release rate. A photoelastic analysis was performed for plate specimens under tension, bending, thermal, and compression loading. The magnitudes of the residual stress fields due to casting and post-curing of the epoxy were determined from the isochromatic patterns of the compression specimens. The elastic residual stresses accounted for approximately 15% of the strain required for crack initiation in a typical tension specimen. A photoelastic analysis of a tension specimen was used to compare plane-stress and plane-strain predictions of maximum shear stress at the center of the bond. This study indicated that a plane-strain assumption is valid at the interface, but at regions remote from the boundary the plane-stress assumption may be more appropriate, since the bond constraint is no longer present.

Strain-gage instrumented specimens were tested in tension, bending, and compression to compare the strain field with that assumed in the theoretical analysis. Result of these studies indicate good agreement with assumed uniform tension, bending, and compression.

Following these studies a number of epoxy-aluminum specimens were cast, where the aluminum bonding surface had received one of four different surface finishes, i.e., polished, glass-peened, milled, or sandblasted, each followed by etching. The polished, glass-peened, and sanblasted surfaces were uniform with respect to surface roughness. The milled surface was nonuniform; it had a rippled appearance, although locally the surface was relatively smooth. The $\mathcal{G}$ measured for these specimens under tension and bending indicated that a sandblasted surface resulted in the highest $\mathcal{G}$ value, followed (in descending order) by the glass-peened, milled, and polished surfaces.

Surface roughness measurements made with a profilometer indicated that the sandblasted surface had the highest roughness, followed by the glass-peened and polished surfaces. Measurements of roughness values for the milled surface varied considerably, but the

lowest values obtained were between those of the glass-peened and polished surfaces. From these data a linear relation was obtained between strain-energy release rate and surface roughness over the range of surfaces examined in this study. Because the crack replicated the surface, greater surface roughness resulted in greater crack area and higher toughness. This implied that $\mathcal{G}$ is dependent on the local character of the surface rather than on the gross nonuniformity present in the milled specimen.

The techniques presented in this report provide a simple method for studying interfacial failure in bonded materials, where one of the materials acts as a relatively rigid body. Results of this investigation have applications in design of bonded structures and in general problems of debonding and delamination between dissimilar bodies. The analysis can be applied to composite materials in analyzing glass–resin interfaces, in bonded joints, and in welded structures where the crack propagates at the interface. This approach can be extended to consider the effects of crack velocity, fatigue loading, environment, and various residual fields on the fracture toughness of bonded materials.

ACKNOWLEDGMENTS

The author wishes to thank Dr. R. N. Vaishnav, Dr. V. Parks, and Dr. A. Thiruvengadam of The Catholic University of America for their guidance and helpful discussions during the course of this investigation. In particular, recognition is due Dr. Parks for his suggestions concerning the experimental phase of this study. The author also wishes to acknowledge the assistance of his colleagues in conducting these studies: Dr. P. W. Mast for discussion and review of the theoretical analysis, Dr. R. J. Sanford for consultation on photoelastic analysis and strain-gage instrumentation, Mr. L. A. Beaubien for assistance in programming the finite-element analysis routines, and Mr. R. W. Thomas for machining specimens and loading fixtures.

REFERENCES

1. M. L. Williams, "The Stresses Around a Fault or Crack in Dissimilar Media," *Bull. Seismol. Soc. Amer.* 49 (2), 199-204, Apr. 1959.
2. F. Erdogan, "Stress Distribution in a Nonhomogeneous Elastic Plane with Cracks," *J. App. Mech.*, Ser. E 30 (2), 232-236 (June 1963).
3. N. I. Muskhelishvili, *Some Basic Problems of the Mathematical Theory of Elasticity*, Translated by J. Radok, P. Noordhoof Ltd., Groningen, The Netherlands, 1953.
4. F. Erdogan, "Stress Distribution in Bonded Dissimilar Materials with Cracks," *J. Appl. Mech.*, Ser. E 32 (2) 403-410 (June 1965).
5. F. Erdogan, "Stress Distribution in Bonded Dissimilar Materials Containing Circular or Ring-Shaped Cavities," *J. Appl. Mech.*, Ser. E 32 (4), 829-836 (Dec. 1965).
6. A. H. England, "A Crack Between Dissimilar Media," *J. Appl. Mech.*, Ser. E 32 (2), 400-402 (June 1965).
7. G. C. Sih and J. R. Rice, "The Bending of Plates of Dissimilar Materials with Cracks," *J. Appl. Mech.*, Ser. E 31 (3), 477-482 (Sept. 1964).

8. J. R. Rice and G. C. Sih, "Plane Problems of Cracks in Dissimilar Media," *J. Appl. Mech.*, Ser. E 32 (2), 418-423 (June 1965).

9. S. G. Sawyer and R. B. Anderson, "Collocated Interfacial Stress Intensity Factors for Finite Bi-Material Plates," *Eng. Fract. Mech.* 4, 605-616 (1972).

10. C. W. Fowlkes, "A Finite Element Analysis of Cracks in the Region of a Bi-Material Interface," *J. Adhesion* 4, 1-36 (1973).

11. K. Lin, "The Stress Intensity of a Crack at an Interface Between Two Materials," Air Force Office of Scientific Research, Technical Report 73-1917, NTIS No. AD 768636, June 1973.

12. T. W. Chou and J. P. Hirth, "Stress Distribution in a Bi-material Plate Under Uniform External Loadings," *J. Compos. Mater.* 4 102-112 (Jan. 1970).

13. E. J. Brown and F. Erdogan, "Thermal Stresses in Bonded Materials Containing Cuts on the Interface," *Int. J. Eng. Sci.* 6, 517-529 (1968).

14. F. Erdogan and G. D. Gupta, "The Torsion Problem of a Disk Bonded to a Dissimilar Shaft," *Int. J. Solids Struct.* 8, 93-109 (1972).

15. M. Gotoh, "Some Problems of Bonded Anisotropic Plates with Cracks Along the Bond," *Int. J. Fract. Mech.* 3 (4), 253-265 (Dec. 1967).

16. D. L. Clements, "A Crack Between Dissimilar Anisotropic Media," *Int. J. Eng. Sci.* 9, 257-265 (1971).

17. J. R. Willis, "Fracture Mechanics of Interfacial Cracks," *J. Mech. Phys. Solids* 19, 353-368 (1971).

18. E. Wu and R. L. Thomas, *Interfacial Fracture Phenomena, Proc. 5th Int. Congr. Rheol.* 1, 575-587, University Park Press, Baltimore, Md., 1969.

19. C. Wang, "Fracture Mechanics for an Interfacial Crack Between Adhesively Bonded Dissimilar Materials," Dep. of Theoretical and Applied Mechanics Report No. 353, University of Illinois at Urbana-Champaign, Mar. 1972.

20. M. L. Williams, "The Continuum Interpretation for Fracture and Adhesion," *J. Appl. Polym. Sci.* 13, 29-40 (1969).

21. M. L. Williams, "The Fracture Threshold for an Adhesive Interlayer," *J. Appl. Polym. Sci.* 14, 1121-1126 (1970).

22. M. L. Williams, "Cohesive-Adhesive Fracture in a Pressurized Double Blister," *J. Adhes.* 5 (1), 81-87 (Jan. 1973).

23. J. D. Burton, W. B. Jones and M. L. Williams, "Theoretical and Experimental Treatment of Fracture in an Adhesive Interlayer," *Trans. Soc. Rheol.* 15 (1), 39-50 (1971).

24. S. J. Bennett, K. L. DeVries, and M. L. Williams, "Adhesive Fracture Mechanics," *Int. J. Fract.* 10, (1) 33-43 (Mar. 1974).

25. L. M. Milne-Thomson, *Plane Elastic Systems*, Springer-Verlag, Berlin, 1960.

26. G. R. Irwin, "Theoretical Aspects of Fracture Failure Analysis," Metals *Eng. Q.* 3 (1), 24-30 (Feb. 1963).

27. E. Orowan, "Fundamentals of Brittle Behavior in Metals," in *Fatigue and Fracture of Metals*, edited by W. M. Murray, M.I.T. Technology Press and John Wiley & Sons, New York, 1952, pp. 139-167.

28. E. Orowan, "The Physical Basis of Adhesion," *J. Franklin Inst.* **290** (6), 493-512 (Dec. 1970).

29. B. A. Boley and J. H. Weiner, *Theory of Thermal Stress*, J. Wiley and Sons, New York, 1960, pp. 429-432.

30. A. Durelli, V. Parks, H. Feng and R. Chiang, "Strains and Stresses in Matrices with Inserts," Mechanics of Composite Systems, Proceedings of 5th Symposium on Naval Structural Mechanics, J. Wendt, H. Liebowitz and N. Perrone, eds., Pergamon Press, New York, 1970, pp. 265-336.

31. S. Mostovoy and E. Ripling, "Fracture Toughness of an Epoxy System," *J. Appl. Polym. Sci.* **10**, 1351-1371 (1966).

32. W. D. Bascom, "Surface Aspects of Bonding Metals with Polymer Adhesives," Polymer Conference Series on Adhesion, University of Utah, Salt Lake City, July 1973.

Appendix A
EXPERIMENTAL PROCEDURE AND ANALYSIS

SPECIMEN PREPARATION

Aluminum-epoxy bimaterial plates were used for this experimental investigation. The aluminum half of the specimen was machined from 2-in.-by-0.375-in. bar stock of 6061-T6 alloy. Various lengths of aluminum plates were machined, depending on the type of loading to be applied to the specimen, as shown in Fig. A1. Aluminum plates eccentrically loaded in compression were 6 in. long, and pin-loaded tensile specimens were 10 in. long. In both cases the epoxy plates were 4 in. in length, 2 in. wide, and 0.375 in. thick.

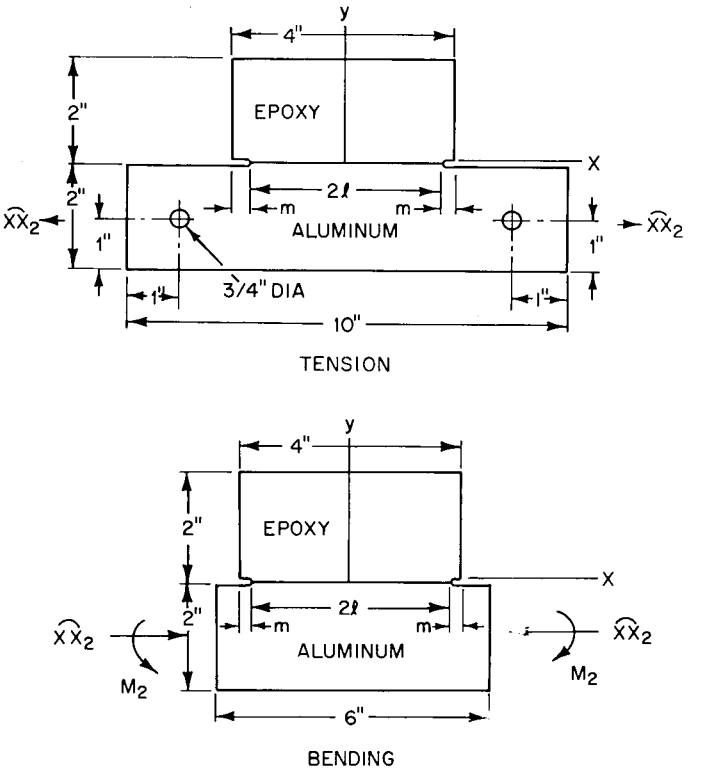

Fig. A1—Specimen geometries and loading conditions

Surface Finish of Aluminum Plates

The aluminum adherends were prepared with four surface finishes; polished; and, as shown in Fig. A2, milled, glass-bead peened, and sandblasted with 60-mesh grit.

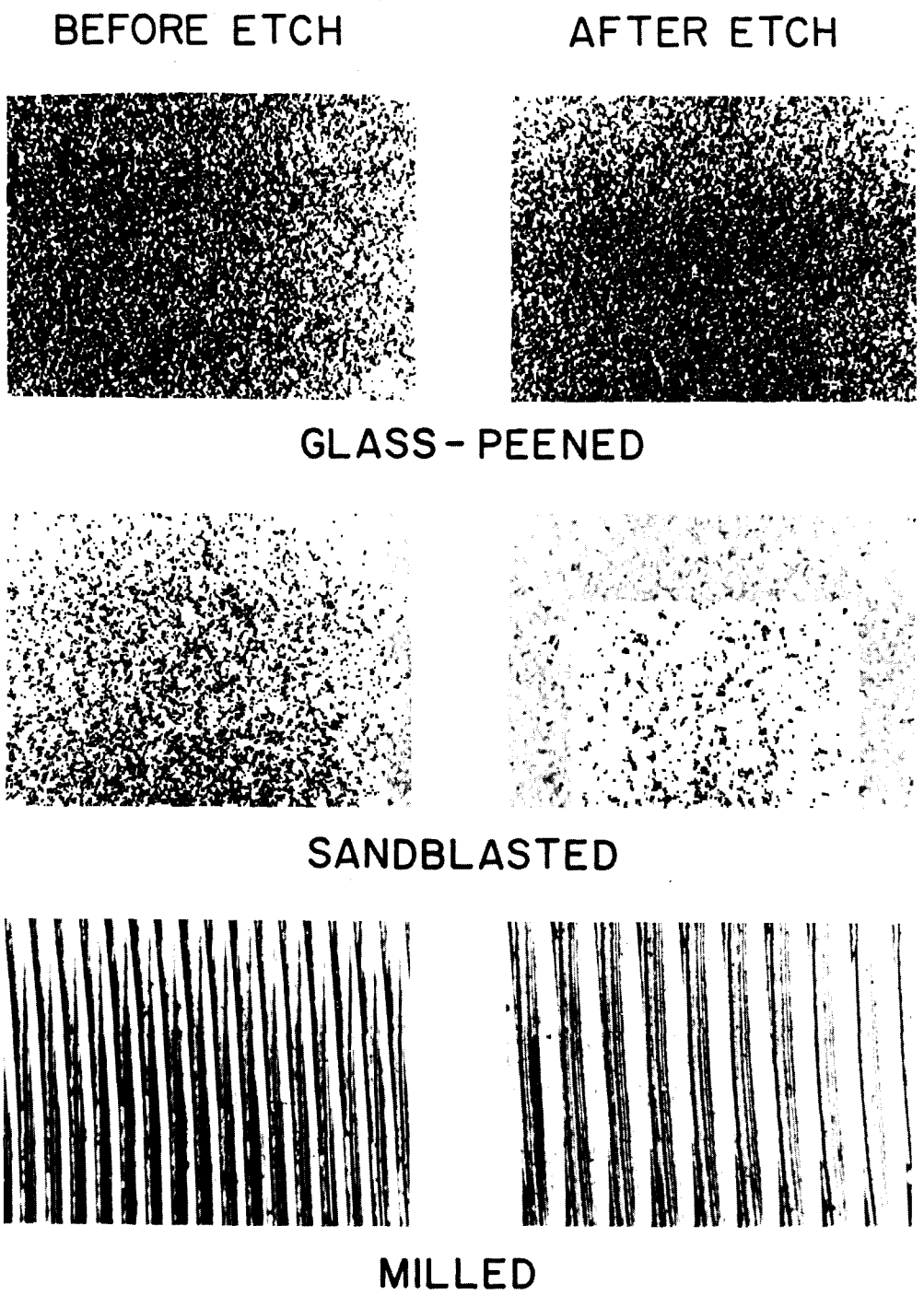

Fig. A2—Aluminum surfaces before and after etching; 30X magnification

Cleaning Process for the Aluminum Plates

The methods used are similar to those now used by the aircraft industry [A1]. The aluminum plate is solvent-cleaned with trichloroethylene and then air-dried to prevent solvent contamination of acid bath used in the next step.

The plate is submerged in an acid bath for 10 min. It is then rinsed in running water and air-dried. The proportional chemical composition of the acid bath (by weight) is 10 parts concentrated sulfuric acid, 1 part sodium dichromate, and 30 parts distilled water. The bath was kept at a temperature of 150° to 155°F.

Epoxy Casting

The aluminum plate was mounted in a mold with inserted Teflon sides and end pieces as shown in Fig. A3. Teflon parts were washed in detergent and air-dried before casting. The epoxy consisted of 100 parts by weight of DER 332 epoxy resin and 12.5 parts by weight of tetraethylene pentamine hardener (TEPA). The mixture was heated to 110°F before casting to remove entrapped air bubbles and decrease viscosity. Solidification occurred in approximately 1 hr, and specimens were subsequently removed from the mold and post-cured at 125°F for 4 hr. After post-curing, a saw cut was made in each end of the epoxy along the interface with a 0.020-in.-thick blade. A razor blade was then used as a wedge to initiate a crack from the sawed notch.

COEFFICIENT OF THERMAL EXPANSION

Values for the thermal expansion of the materials used in this investigation were determined using a quartz-tube dilatometer. Displacement of the quartz tube was measured with a differential transformer over a range of temperatures from 0°F to 150°F. The dilatometer was immersed in a stationary bath of silicone oil (Dow Corning 200) for the series of tests below room temperature and in a circulating bath of silicone oil for the series of measurements above room temperature. In each case the temperature of the bath was monitored with an iron-constantan thermocouple immersed in the bath next to the test sample. Temperature rates for the data presented here were approximately 15°F per hour.

A plot of displacement vs temperature is shown in Fig. A4 for the aluminum and the epoxy post-cured at 125°F for 4 hr. The slopes of these curves normalized by specimen length are measures of the coefficient of thermal expansion in microinches per inch per degree Fahrenheit. The epoxy specimen was 1.725 in. long, and the aluminum specimen was 2.503 in. long. Measured values for the aluminum ranged from 11.1 μin./in.($^\circ F^{-1}$) for 0°F to 68°F to 12.4 μin./in.($^\circ F^{-1}$) for 68°F to 150°F. These values are slightly lower than the values, reported in Refs. A2 and A3, of 12.1 μin./in.($^\circ F^{-1}$) for -58°F to 68°F and 13.0 μin./in.($^\circ F^{-1}$) for 68°F to 212°F. Values for the epoxy ranged from 31.1 μin./in.($^\circ F^{-1}$) for 0°F to 68°F to 38.9 μin./in.($^\circ F^{-1}$) for 68°F to 150°F. These values are within the range, reported in Ref. A4, expected for unfilled epoxy.

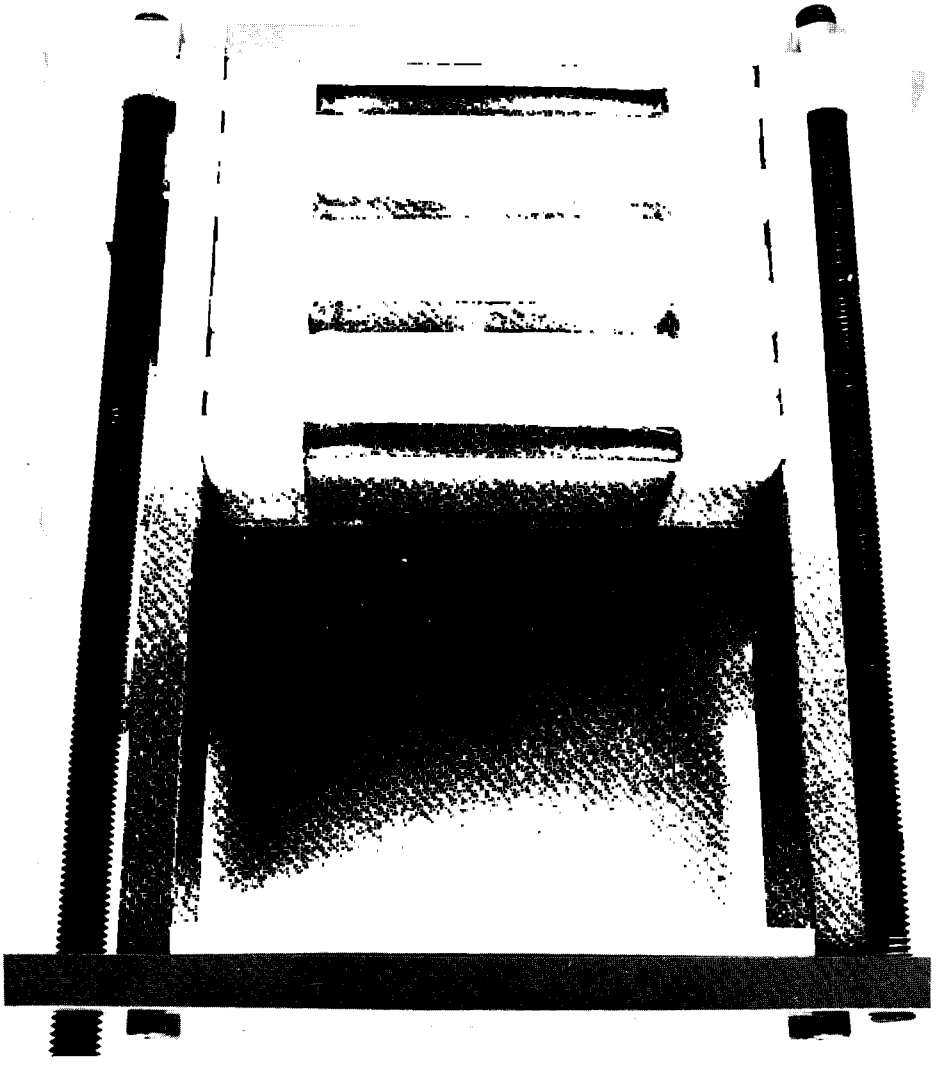

Fig. A3—Mold assembly for casting specimens

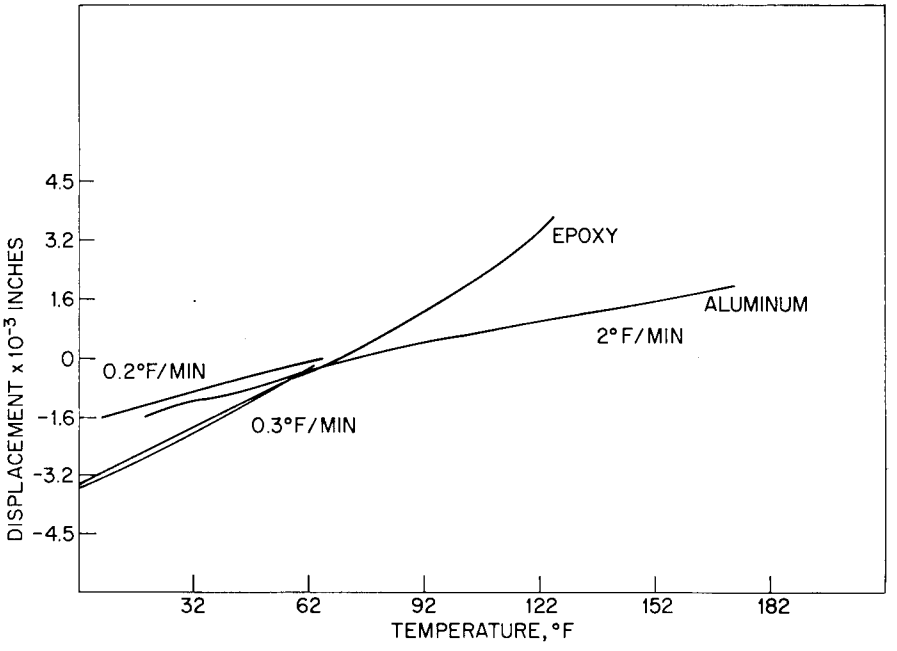

Fig. A4—Thermal-expansion data for aluminum and epoxy

MATERIAL PROPERTIES

Values for the Young's modulus E and Poisson's ratio ν for 6061-T6 aluminum, obtained from Refs. A2 and A3, are $E = 10^7$ psi and $\nu = 0.33$. For epoxy materials, broad ranges of properties are possible, depending on hardener concentrations and post-curing conditions [A5,A6]. To determine E and ν for the particular resin system and curing conditions used in this investigation, a disk was machined from a cast-epoxy plate. Strain gages were mounted at the center of each side of the disk, one along the 0° or loading direction and the other at 90° or perpendicular to the loading direction (Fig. A5). Analysis of the strain-gage data under several cycles of loading yielded values of $E = 5.7 \times 10^5$ psi and $\nu = 0.34$. These values included a 2% correction for the transverse sensitivity of the gages [A5], necessary because of the biaxial nature of this stress field.

The same disk used in the determination of material properties was used to determine the material fringe value [A7]. A series of photographs of both light- and dark-field isochromatic patterns (Fig. A6) were used to obtain the data shown in Fig. A7. The material fringe value determined from these data was 51.9 psi-in./fringe.

FINITE-ELEMENT ANALYSIS

A numerical analysis was made of the bonded-joint specimen configuration using a two-dimensional finite-element program. This program was developed by Swedlow [A8] at Carnegie-Mellon University and has been adapted to run on NRL's CDC 3800 computer

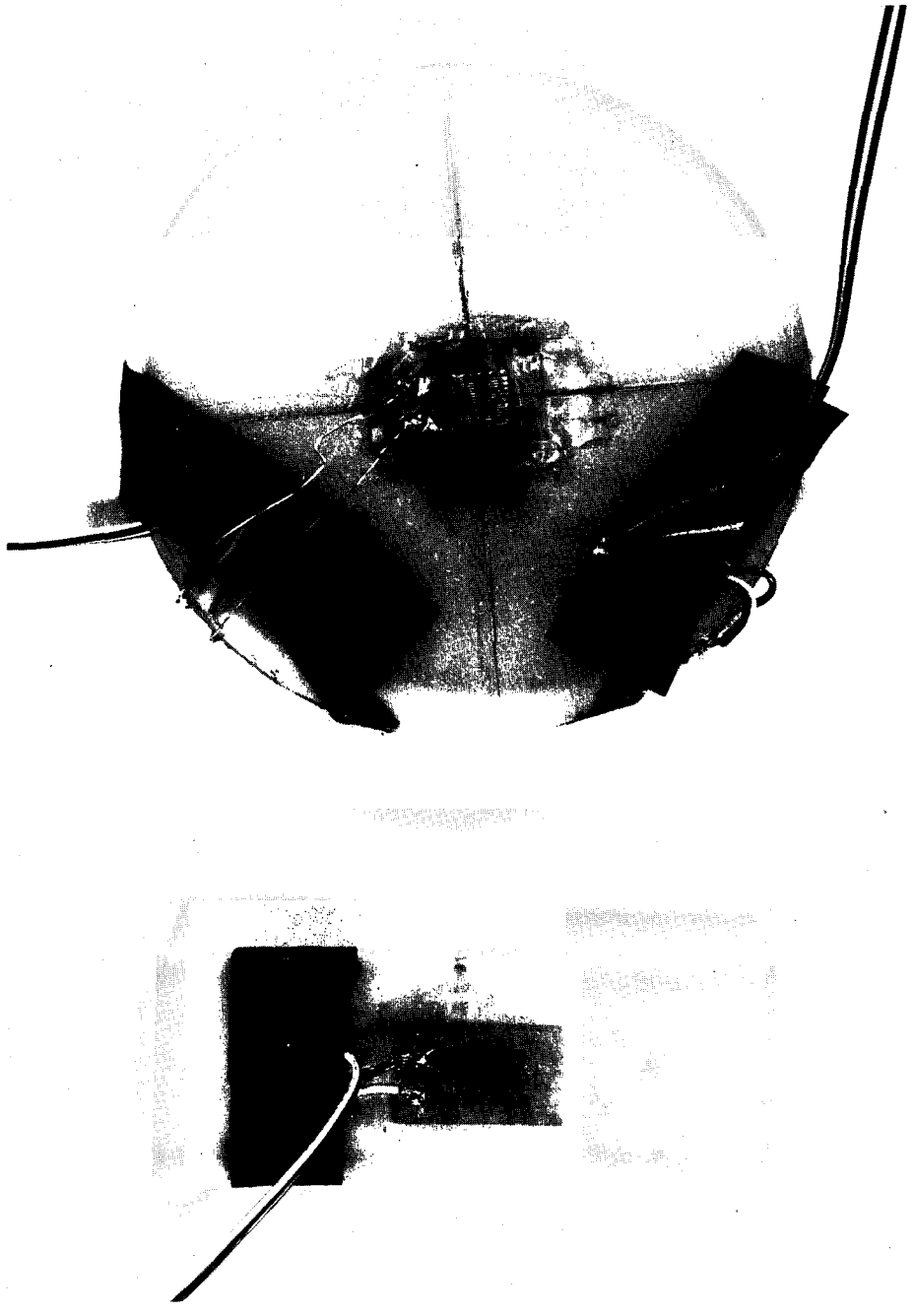

Fig. A5—Strain-gage locations for a disk in diametral compression

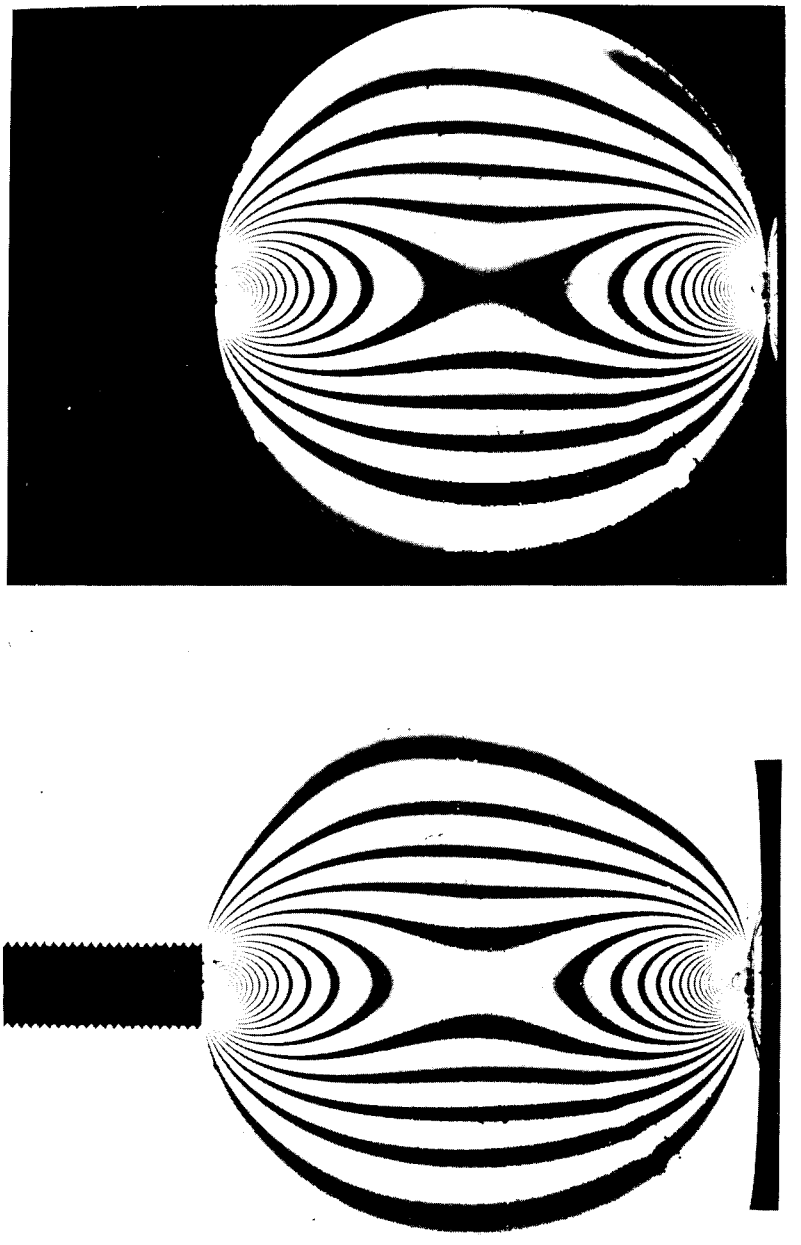

Fig. A6—Isochromatic patterns for a disk in diametral compression

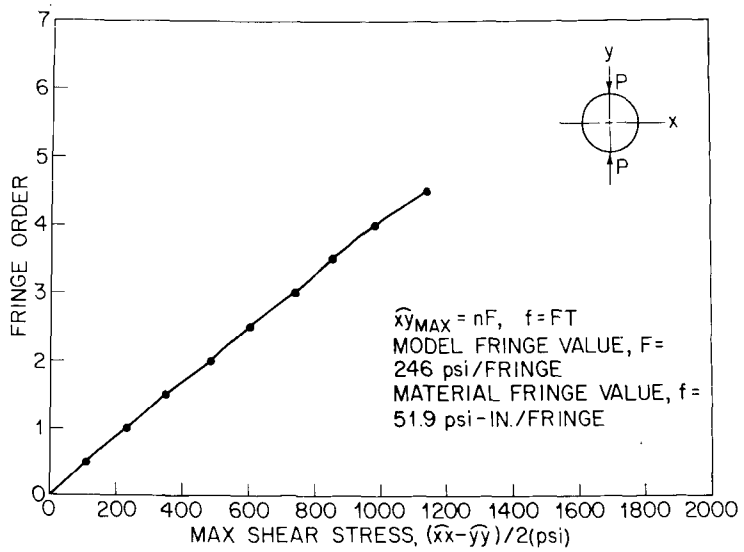

Fig. A7—Fringe order vs shear stress for disk specimen

system. Certain modifications to the original program were required, to permit the solution of nonhomogeneous problems as well as to provide plotting capabilities.

A computer plot of the grid system used for this problem is shown in Fig. A8. Elements were removed from the upper half plane along the boundary to simulate crack growth.

A comparison of the normal and shear stresses along the interface computed by this analysis with the theoretical solution is shown in Fig. A9 and A10. From these results it appears that the analytical solution to this problem agrees well with finite-element analysis at regions remote from the crack tip.

REFERENCES

A1. N. J. De Lollis, *Adhesive for Metals*, Industrial Press, New York, 1970.

A2. *Alcoa Aluminum Handbook*, Aluminum Co. of America, Pittsburgh, Pa., 1959.

A3. *Aerospace Structural Metals Handbook*, vol. II, "Non-Ferrous Alloys," Syracuse University Press, Syracuse, N.Y., 1970.

A4. H. Lee and K. Neville, *Handbook of Epoxy Resins*, McGraw-Hill Book Co., New York, 1967.

A5. C. C. Perry and H. R. Lissner, *The Strain Gage Primer*, 2d ed., McGraw-Hill Book Co., New York, 1962.

A6. S. Mostovoy and E. Ripling, "Fracture Toughness of an Epoxy System," *J. Appl. Polym. Sci.* 10, 1351-1371 (1966).

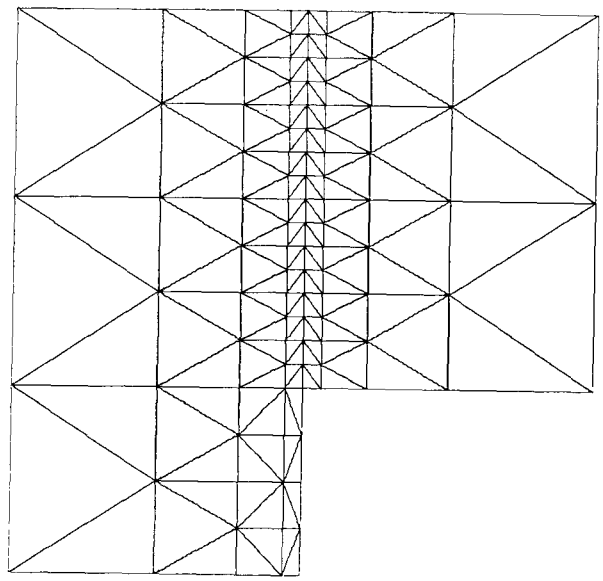

Fig. A8—Finite-element grid used to analyze bonded plate specimen

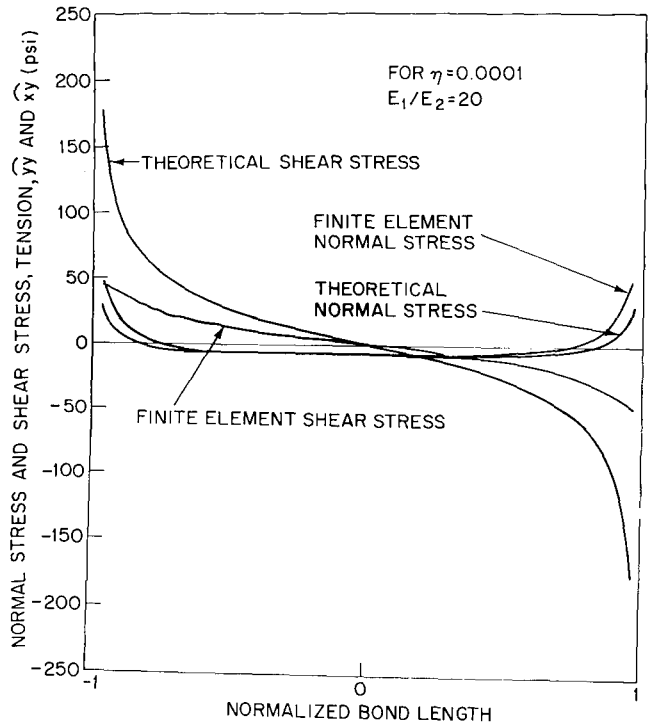

Fig. A9—Comparison of finite-element results with theoretical analysis for tension specimen

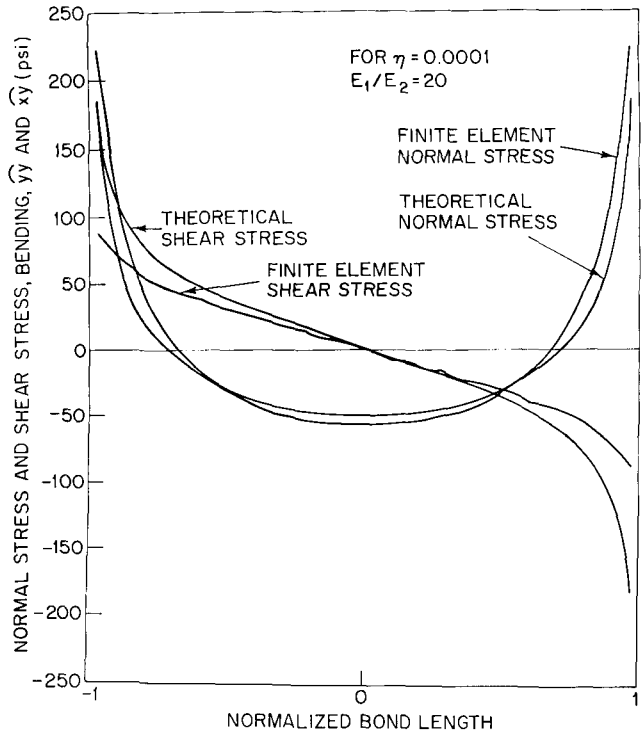

Fig. A10—Comparison of finite-element results with theoretical analysis for bending specimen

A7. M. Frocht, *Photoelasticity*, vol. II, John Wiley & Sons, New York, 1961.

A8. J. Swedlow, "Information for Users of Finite Element Programs," Report SM-33A, Department of Mechanical Engineering, Carnegie Institute of Technology, Carnegie-Mellon University, Pittsburgh, Pa., Feb. 1971.